POLITECNICO
MILANO 1863

SCUOLA DI INGEGNERIA INDUSTRIALE
E DELL'INFORMAZIONE

Finding regions of bounded motion in binary asteroid environments using Lagrangian descriptors

Tesi di Laurea Magistrale in
Space Engineering

Author: **Sebastiano Raffa**

Student ID: 925192
Advisor: Prof. Francesco Topputo
Co-advisor: Gianmario Merisio
Academic Year: 2020-21

Abstract

Trajectories design in chaotic environments, such as the Didymos–Dimorphos binary asteroid system, is challenging as it requires the use of high-fidelity models in which periodic solutions vanish.

Lagrangian descriptors are investigated in this work as a tool for finding regions of bounded motion around the secondary Dimorphos, for a certain period of time. To this end, distant retrograde orbits are calculated in the simplified planar circular restricted three-body problem, and their initial conditions are inspected against the Lagrangian descriptors fields for classification of the behavior of the regions that is a priori unknown.

The same procedure is repeated for the spatial case, in which the periodic planar orbits are continued out of the plane to generate resonant periodic three-dimensional orbits: their initial conditions will belong to areas of the scalar field containing similarly evolving orbits. On the other hand, other regions will contain orbits that escape the vicinity of Dimorphos or likely impact with it. Once classified, their evolution is observed in more representative models, and an attempt is made to find bounded solutions through phase space sampling.

Bounded orbits exist, for the selected search space, in all cases but at the pericenter of the heliocentric orbit, where the solar radiation pressure contribution is so high to sweep away the vast region of bounded motion.

The results, therefore, confirm the capability of Lagrangian descriptors to organize the phase space into regions of qualitatively different motion and are more convenient than other chaos indicators as they do not require the propagation of the variational equations.

Keywords: Bi-elliptic restricted 4-body problem, Lagrangian descriptors, Didymos binary asteroid, bounded motion region

Sommario

La progettazione di traiettorie in ambienti caotici, come nel caso del sistema di asteroidi binari Didymos–Dimorphos, risulta impegnativa in quanto richiede l'uso di modelli ad alta fedeltà in cui soluzioni periodiche svaniscono.

I descrittori Lagrangiani sono analizzati in questo lavoro come strumento per trovare regioni dello spazio delle fasi in cui il movimento di un satellite risulta confinato attorno a Dimorphos, per un certo periodo di tempo. A tal fine, orbite retrograde distanti attorno a Dimorphos sono calcolate nel modello planare circolare ristretto a tre corpi e le loro condizioni iniziali sono confrontate rispetto al campo scalare generato dai descrittori Lagrangiani, per la classificazione del comportamento delle varie regioni che, a priori, è sconosciuto. La stessa procedura viene ripetuta per il caso tridimensionale, in cui le orbite planari periodiche vengono continuate fuori dal piano per generare orbite tridimensionali periodiche risonanti: le loro condizioni iniziali apparterranno ad aree del campo scalare contenenti orbite con evoluzione simile. D'altro canto, altre regioni contengono orbite che fuggono dalle vicinanze di Dimorphos o probabilmente impattano con esso. Una volta classificate, se ne osserva l'evoluzione in modelli più rappresentativi e si tenta di trovare soluzioni confinate attorno a Dimorphos attraverso il campionamento dello spazio delle fasi.

Orbite confinate esistono, per lo spazio di ricerca selezionato, in tutti i casi tranne che al pericentro dell'orbita eliocentrica, dove il contributo della pressione di radiazione solare è così alto da spazzare via la vasta regione di movimento confinato.

I risultati, quindi, confermano la capacità dei descrittori lagrangiani di organizzare lo spazio delle fasi in regioni di moto qualitativamente diverso e sono più convenienti di altri indicatori di caos in quanto non richiedono la propagazione delle equazioni variazionali.

Parole chiave: Problema biellittico dei quattro corpi ristretto, descrittori Lagrangiani, asteroide binario Didymos, regioni di movimento confinato

Ringraziamenti

A conclusione di questo percorso di tesi, mi sento di dedicare alcune righe a quelle persone che hanno avuto un ruolo chiave al raggiungimento di questo risultato.

Ringrazio Gianmario Merisio, angelo custode durante tutte le fasi di questo lavoro, per la sua rassicurante presenza e completa disponibilità.

Ringrazio il Prof. Francesco Topputo, il quale mi ha introdotto a questo nuovo mondo, fornendomi gli strumenti necessari a muovere i primi passi.

Siete entrambi fonte d'ispirazione.

Ringrazio i miei genitori, nonché miei modelli, per avermi supportato (sopportato) durante questi anni di formazione, il vostro contributo è stato essenziale.

Ringrazio mia sorella, sorgente infinita di saggezza e perenne spalla su cui contare. Sarai sempre la numero uno per me.

Ringrazio Marcolino, Delia, Salvo ed Elisa per aver contornato le mirabolanti giornate di stesura con leggerezza e spensieratezza; non avrei potuto immaginare compagnia migliore.

Ringrazio Alicina per essermi stata sempre vicina in questo viaggio, sopratutto nei momenti in cui tutto sembrava più grande di me. Sei stata un tassello fondamentale, spronandomi a tirar fuori il meglio di me.

Infine, come disse Snoop Dogg:
"Last but not least, I wanna thank me, I wanna thank me for believing in me, I wanna thank me for doing all this hard work, I wanna thank me for having no days off, I wanna thank me for never quitting".

"I would like to die on Mars. Just not on impact." - Elon Musk

Contents

Abstract **i**

Sommario **iii**

Ringraziamenti **v**

Contents **vii**

List of figures **1**

List of tables **3**

List of acronyms **5**

1 Introduction **7**

1.1 Context 7

1.2 Motivation 7

1.3 Objectives and research questions 8

1.4 Structure of the thesis 8

2 Literature review **11**

2.1 The circular restricted three-body problem 12

2.1.1 Equations of motion 12

2.1.2 Energy integral and Jacobi constant 13

2.1.3 Hill's region 13

2.1.4 Equilibrium points 14

2.1.5 Motion near the collinear equilibrium points 15

2.1.6 Trajectory design 18

2.2 Elliptic restricted three-body problem 22

2.3 Chaos Indicators 23

2.3.1 Finite-time Lyapunov exponents 23
2.3.2 Variational theory 24
2.3.3 Lagrangian descriptors 26
2.3.4 Qualitative trade-off 27

3 Modeling of the dynamical environment 29
3.1 Didymos–Dimorphos binary system 29
3.2 Dynamical regimes 29
3.3 Equations of motion 30
3.3.1 Fourth-body perturbation 32
3.3.2 Solar radiation pressure 33

4 Methodology 35
4.1 Application of Lagrangian descriptors to astrodynamics 35
4.2 Finding regions of bounded motion 36
4.3 Periodic orbit research 37
4.3.1 Distant retrograde orbits 37
4.3.2 Spatial resonant periodic orbits 38

5 Results 41
5.1 Investigation in the circular restricted three-body problem 41
5.1.1 Lagrangian descriptors comparison 41
5.1.2 Final true anomaly dependence 43
5.1.3 Classification of regions in the planar case 45
5.1.4 Classification of regions in the three-dimensional case 46
5.2 Bounded orbits through phase space sampling 48
5.2.1 Sampling in the circular restricted three-body problem 49
5.2.2 Sampling in the elliptic restricted three-body problem 52
5.2.3 Sampling in the bi-elliptic restricted four-body problem 55
5.2.4 Sampling in the perturbed bi-elliptic restricted four-body problem . 58

6 Final remarks 67

Bibliography 69

List of figures

2.1 CR3BP reference systems 12
2.2 The five cases of the Hill's region. 14
2.3 Lagrangian points for the Earth–Moon system. 15
2.4 Flow in the equilibrium region 17
2.5 Flow in the position region 17
2.6 Globalization of the manifolds 20
2.7 ER3BP, primary and secondary 22
2.8 Material surface, tangent, and normal spaces 25

3.1 Main accelerations in the Didymos–Dimorphos system 30

5.1 LD in comparison for a $f_f = 5\pi$. 42
5.1 LD in comparison for a $f_f = 5\pi$. 43
5.2 M_1 and M_v in comparison for different values of f_f. 44
5.3 DROs 45
5.4 M_1 field of the planar CR3BP 46
5.5 Resonance ratios as function of the x coordinate 47
5.6 Resonant orbits for different values of n/k 48
5.7 LD M_1 in the CR3BP at different z slices. 49
5.8 M_1 sampling in the CR3BP 50
5.9 Samples evolution in the CR3BP 52
5.10 LD M_1 in the ER3BP at different z slices. 52
5.11 M_1 sampling in the ER3BP 53
5.12 Samples evolution in the ER3BP 55
5.13 LD M_1 in the BER4BP, for $\theta_0 = 0$, at different z slices. 55
5.14 M_1 sampling in the BER4BP, $\theta_0 = 0$ 56
5.15 Samples evolution in the BER4BP 58
5.16 LD M_1 in the SRP perturbed BER4BP at different z slices, for $\theta_0 = 0$. . . 59
5.17 M_1 sampling in the SRP perturbed BER4BP, $\theta_0 = 0$ 60
5.18 Samples evolution in the SRP perturbed BER4BP, $\theta_0 = 0$ 62

5.19 LD M_1 in the SRP perturbed BER4BP at different z slices, for $\theta_0 = \pi$. . . 62
5.20 M_1 sampling in the SRP perturbed BER4BP, $\theta_0 = \pi$ 63
5.21 Samples evolution in the BER4BP, $\theta_0 = \pi$ 65

List of tables

2.1 Families of LDs 27
2.2 Qualitative comparison of chaos indicators. 28

3.1 Parameters cannonball model. 32
3.2 Physical parameters of the Didymos–Dimorphos system 34

4.1 List of LDs. 36

5.1 Grid width parameters 41
5.2 Resonances selected 47
5.3 Orbits ICs in the CR3BP. 50
5.4 Orbits ICs in the ER3BP. 53
5.5 Orbits ICs in the BER4BP, $\theta_0 = 0$. 57
5.6 Orbits ICs in the SRP perturbed BER4BP, for $\theta_0 = 0$. 60
5.7 Orbits ICs in the SRP perturbed BER4BP, for $\theta_0 = \pi$. 64

List of acronyms

AIDA Asteroid Impact and Deflection Assessment.

BER4BP bi-elliptic restricted four-body problem.

CR3BP circular restricted three-body problem.

DRO distant retrograde orbit.

EoM equations of motion.

ER3BP elliptic restricted three-body problem.

FTLE finite-time Lyapunov exponent.

IC initial condition.

LCS Lagrangian coherent structure.

LD Lagrangian descriptor.

PBER4BP perturbed bi-elliptic restricted four-body problem.

PCR3BP planar circular restricted three-body problem.

PECE predictor-corrector.

SRP solar radiation pressure.

STM state transition matrix.

VSVO variable-step, variable-order.

1 Introduction

1.1. Context

Small solar system objects, such as asteroids and comets, are residual debris from the creation of the inner solar system, including our planet. As their chemical structure has remained unchanged since their formation, such objects are thought to have a composition that is very similar to that of the Earth during its early stages of formation. For this reason, they are thought to hold the key to a better understanding of the origins of life.
In the upcoming years, two missions part of the Asteroid Impact and Deflection Assessment (AIDA) international collaboration are scheduled to visit the (65803) Didymos binary system to investigate and demonstrate the kinetic effects of an impactor colliding with the minor body Dimorphos: NASA's DART, and ESA's Hera.
The present work aims at finding regions of the phase space in which the motion of the spacecraft remains in the vicinity of Dimorphos, regardless of the perturbations. These results can be useful to fulfill a variety of science objectives, for instance, the global mapping of gravitational fields as well as the study of their chemical composition.

1.2. Motivation

Bounded motion can be achieved through periodic or quasi-periodic orbits. The latter have many of the same advantages as periodic orbits, as well as a few additional benefits. Five-dimensional stable and unstable manifolds exist for two-dimensional hyperbolic invariant tori with quasi-periodic motion on their surfaces. Periodic orbit families, on the other hand, typically have three-dimensional stable and unstable manifolds [28]. As a result, including quasi-periodic orbits in space missions design greatly expands the design space to meet mission constraints and science objectives. Solving a system of partial differential equations or shooting algorithms using surfaces of section or a stroboscopic map are two common methods for computing invariant tori [1]. In the phase space, quasi-periodic motions are much more prevalent, but their computation entails additional complexities. For this reason, a novel methodology based on Lagrangian descriptors (LDs) is presented,

which allows for a straightforward, indirect method of searching for quasi-periodic orbits in highly chaotic environments by separating the phase space in regions with qualitatively different behavior.

1.3. Objectives and research questions

Research Questions. Didymos is a sub-kilometer asteroid and, together with its small minor companion Dimorphos, forms a binary system orbiting the Sun. Due to the numerous disturbances, the environment in its vicinity is highly chaotic, making it difficult to identify regions of space where the satellite's motion remains bounded.
The present work aims to answer the following research question:

- *To what extent do Lagrangian descriptors provide insight into the highly chaotic environment by revealing the structures that organize the phase space into regions of different behavior?*

Research Objective. The final objectives of this dissertation are:

- *Find regions of bounded motion around the Didymos-Dimorphos binary system for a certain amount of time.*
- *Investigate the capability of the different Lagrangian descriptors to reveal organizing structures in astrodynamics systems.*
- *Classify the identified regions according to their qualitative behavior.*

1.4. Structure of the thesis

The remainder of this work is organized as follows

1. Chapter 1 presents the motivation, as well as the objectives and the research question;
2. Chapter 2 offers an overview of the literature on the investigated topics, providing a background for a complete understanding;
3. Chapter 3 introduces and models the dynamical environment in the vicinity of the Didymos–Dimorphos binary system;
4. Chapter 4 shows the adopted methodology and the algorithms to find and classify the regions of the scalar LD field;
5. Chapter 5 explains and discusses the results;

6. Chapter 6 draws conclusions and presents insight to further expand this work.

2 | Literature review

One of the oldest problems in the field of dynamical systems is the three-body problem. Indeed, Isaac Newton first formulated it in 1687 in the *Philosophiæ Naturalis Principia Mathematica*. He did not solve the problem: the knowledge of a general solution would be required to solve it, which is impossible to obtain as it turned out. Euler later considered the problem of three bodies lying on the same line in his *De motu rectilineo trium corporum se mutuo attrahentium*, in 1767. He also studied the problem in a co-rotating reference frame with the origin at the barycentre. This promoted the development of the circular restricted three-body problem (CR3BP).

Several authors, including Lagrange, Laplace, Jacobi, Poincaré, Birkhoff, and others, contributed to the extension and analysis of such a problem. Lagrange demonstrated, in particular, that for any two masses in circular orbits, there are five equilibrium points, now known as *Lagrangian points*: these are special locations where the gravitational forces of the bodies balance the centrifugal forces. Small objects in orbit at Lagrange points remain in equilibrium relative to the large bodies, the so-called *primaries*.

In 1836, Jacobi proved the existence of a quantity conserved throughout motion: the integral of motion, also known as the *Jacobi integral*. George William Hill later used this knowledge to introduce the zero-velocity curves (ZVC), which are regions where the body is allowed to move. A feature of the CR3BP, an autonomous dynamical system (i.e., it does not explicitly depend on time) when modeled in a rotating frame, is the presence of *channels* in the phase space that allow global transport mechanisms: *invariant manifolds*. These structures can be obtained by analyzing stable and unstable manifolds of a periodic solution. Their importance lies in the possibility of exploiting such space channels to design space missions that use very little fuel.

If the primaries move in an elliptical orbit, this model no longer works, and the eccentricity of the orbit must be accounted for in a more complex model, namely the elliptic restricted three-body problem (ER3BP). Because the distance between the primaries is no longer constant and the reference frame does not rotate uniformly, the system is no longer autonomous.

2.1. The circular restricted three-body problem

2.1.1. Equations of motion

Problem Description. Consider the motion of an object P moving in a gravitational field generated by two bodies, m_1 and m_2, respectively the *primary* and the *secondary*. This problem can be simplified if the following two conditions are met, restricting the analysis to the circular restricted three-body problem:

1. the mass of the object is significantly smaller than that of the other two: its influence on their motion is negligible;
2. primary and secondary orbit around their barycentre on circular orbits.

Let's consider two coordinates systems, one inertial (X, Y, Z) and the other one (x, y, z) as rotating, with constant speed, around the first (Fig. 2.1). Masses m_1 and m_2 refer to the largest and smallest mass, respectively. They are located on fixed positions on the rotating $x-$axis. The system is made non-dimensional selecting units of time, length, and mass. It can be fully described through the **mass parameter $\boldsymbol{\mu}$**, defined as follows

$$\mu = \frac{m_2}{m_1 + m_2}. \tag{2.1}$$

The unit of length is the constant distance between m_1 and m_2: the positions of the primary and secondary on the rotating $x-$axis are $(-\mu, 0, 0)$ and $(1-\mu, 0, 0)$, respectively. The time unit is such that one orbital period corresponds to 2π. Finally, the unit of mass is taken as the sum of m_1 and m_2.

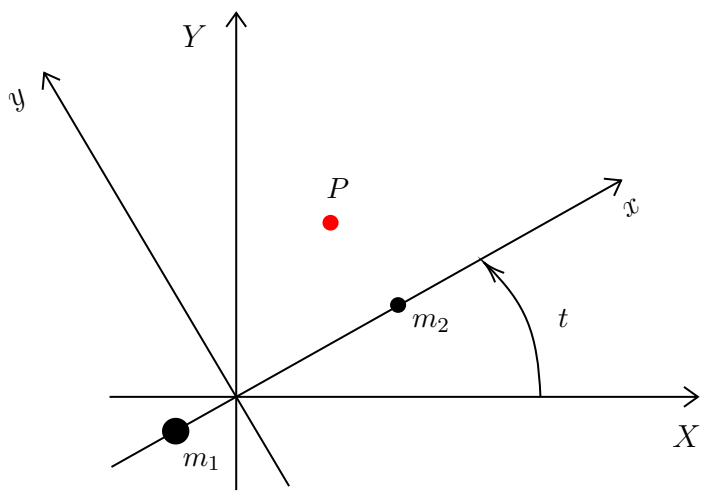

Figure 2.1: Reference systems: inertial and rotating. They share the same z-axis position.

When derived in the inertial frame (X, Y, Z), the total energy of the system is not conserved therefore the system of differential equations is not Hamiltonian, and the energy integral is **time-varying**. If the motion of P is instead expressed in the rotating frame (x, y, z), the equations of motion (EoM) are autonomous and yield a **constant** integral of motion. The Euler–Lagrange equation is applied to derive the set of the three differential equations governing the motion of P [20]

$$\begin{aligned} \ddot{x} - 2\dot{y} &= -\Omega_x, \\ \ddot{y} + 2\dot{x} &= -\Omega_y, \\ \ddot{z} &= -\Omega_z, \end{aligned} \tag{2.2}$$

where

$$\Omega(x, y) = -\frac{1}{2}(x^2 + y^2) - \frac{\mu_1}{r_1} - \frac{\mu_2}{r_2} - \frac{1}{2}\mu_1\mu_2, \tag{2.3}$$

is the **effective potential**. The subscript $\Omega_{(\cdot)}$ denotes the derivative with respect to the variable $(\cdot)$. The magnitudes of the position vectors r_1 and r_2 are the distances of P in the rotating frame from m_1 and m_2, respectively, given by

$$r_1 = \sqrt{(x+\mu)^2 + y^2 + z^2}, \quad \text{and} \quad r_2 = \sqrt{(x-1+\mu)^2 + y^2 + z^2}. \tag{2.4}$$

2.1.2. Energy integral and Jacobi constant

In the CR3BP, the energy integral is the only known integral of motion and represents a very effective tool for characterizing the regions of space in which, once the initial conditions have been fixed, motion is possible or not. Its expression reads [20]:

$$E(x, y, z, \dot{x}, \dot{y}, \dot{z}) = \frac{1}{2}(\dot{x}^2 + \dot{y}^2 + \dot{z}^2) + \Omega = \frac{1}{2}v^2 + \Omega. \tag{2.5}$$

It is strictly related with the **Jacobi integral** C, being $C = -2\,E$.

2.1.3. Hill's region

The motion of the object P is always confined to the Hill's region of the corresponding Jacobi energy C. Considering Eq. (2.5), if the velocity v is set to zero for a certain initial condition, then the value of the critical energy E^* is obtained [2]. In the same way, the critical Jacobi constant C^* is obtained by setting to zero the velocity in $C = -v^2 - 2\,\Omega$:

$$\text{Allowed regions:} \quad C \leq C^* \text{ or } E \geq E^* \text{ as } v^2 \geq 0 \tag{2.6}$$

$$\text{Forbidden regions:} \quad C > C^* \text{ or } E < E^* \text{ as } v^2 < 0. \tag{2.7}$$

Depending on the value of the Jacobi constant (or, equivalently, of the energy), five scenarios can be laid out, defining the so-called **realms** of possible motion. As an example, these regions are obtained for the Earth–Moon case and shown in Fig. 2.2: the area in grey is the forbidden one, where the motion of the spacecraft is not physically possible.

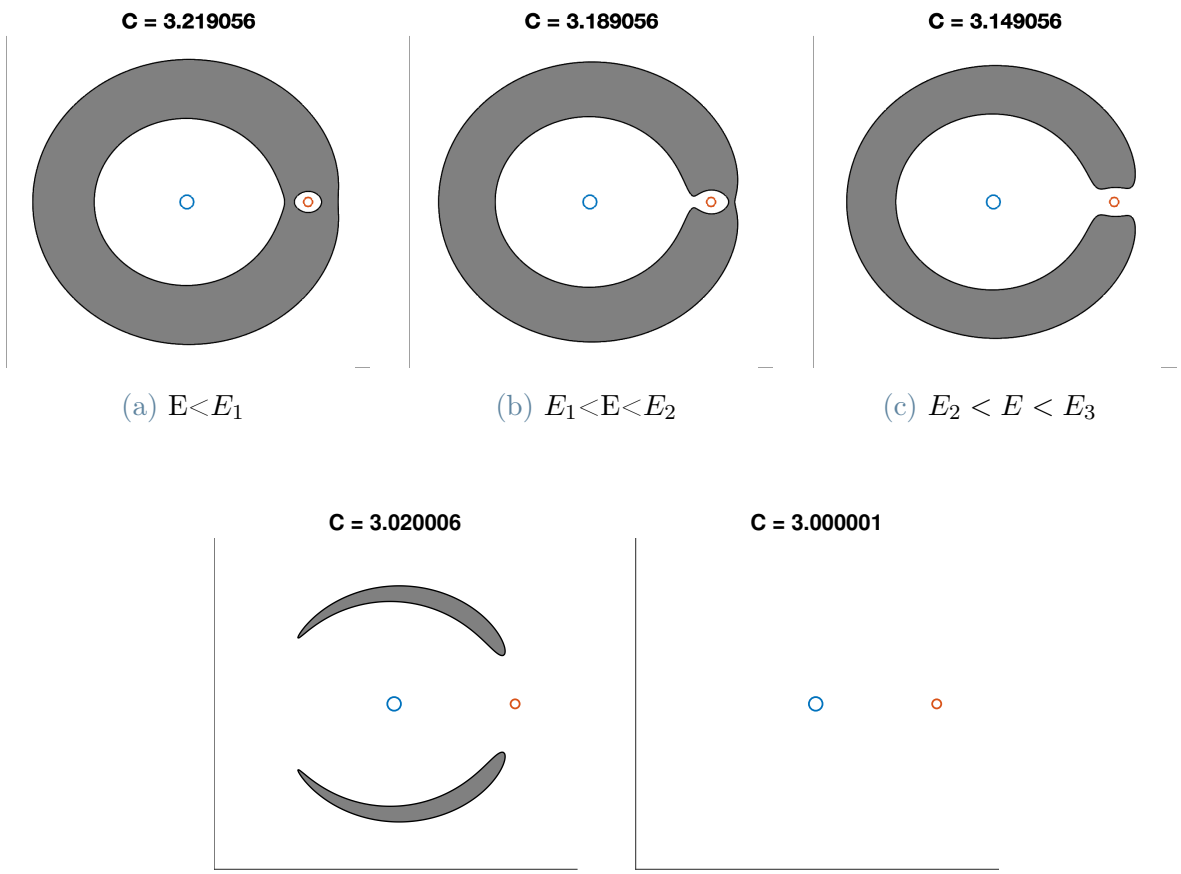

(a) E<E_1 (b) E_1<E<E_2 (c) $E_2 < E < E_3$

(d) $E_3 < E < E_4$ (e) $E < E_4$

Figure 2.2: The five cases of the Hill's region.

2.1.4. Equilibrium points

Lagrange found out the presence of five specific regions in space, called **Lagrangian points**: an object placed there would have zero velocity and zero acceleration, meaning that small objects would permanently appear at rest relative to the primaries. Let's consider the planar case. Rearranging Eqs. 2.2 in their first-order form would lead to [20]:

$$
\begin{aligned}
\dot{x} &= v_x \\
\dot{y} &= v_y \\
\dot{v_x} &= 2v_y - \Omega_x \\
\dot{v_y} &= -2v_x - \Omega_y.
\end{aligned}
\tag{2.8}
$$

To find the equilibrium point of the system it is required that $\dot{\mathbf{x}} = 0$, that is:

$$
v_x = v_y = \dot{v_x} = \dot{v_y} = 0. \tag{2.9}
$$

As an example calculation, these points are computed for the Earth–Moon system and shown in Fig. 2.3. Positions L1, L2, and L3 are unstable: any object orbiting these regions will tend to **fall out** the orbit; this trend, for spacecraft populating these areas, must be actively counter-acted with maneuvers. On the other hand, points L4 and L5 are stable: objects are being **pulled** into them so that no station-keeping would be needed.

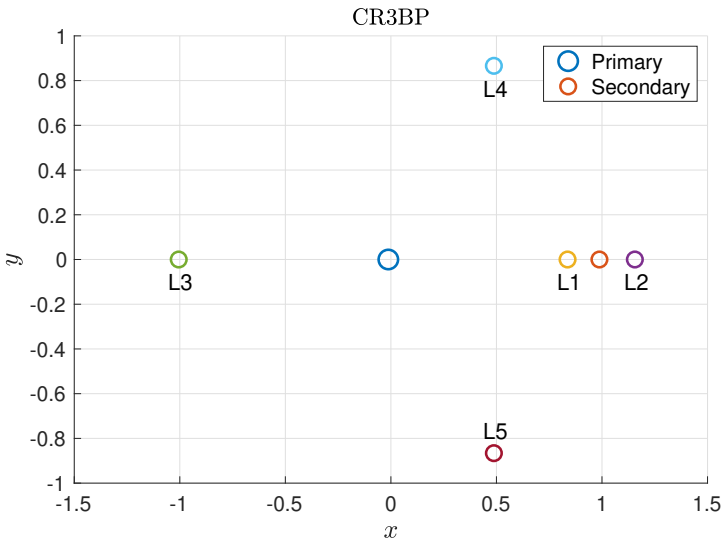

Figure 2.3: Lagrangian points for the Earth–Moon system.

2.1.5. Motion near the collinear equilibrium points

Let's investigate, for the planar case, the flow near the collinear equilibrium points. After the linearization of the equations around the equilibrium solution, it is possible to compute the eigenvalues and corresponding eigenvectors [20].

To better visualize the orbit structure on the 4-dimensional phase space, a change of coordinate system is carried out: the eigenvectors $(\boldsymbol{\xi}, \boldsymbol{\eta}, \boldsymbol{\zeta_1}, \boldsymbol{\zeta_2})$ are used as the new axes

for the reference frame. After the coordinates change, the energy integral of the linearized system takes the form [20]

$$E_l = \lambda\xi\eta + \frac{\nu}{2}(\zeta_1 + \zeta_2), \tag{2.10}$$

where the eigenvalues of the linearized system are $\pm\lambda$ and $\pm i\nu$.
Solutions such that $E_l = \epsilon > 0$ correspond to the case in which the Hill's region includes a neck around the Lagrangian point. By imposing $E_l = \epsilon$, Eq. (2.10) becomes:

$$\frac{\lambda}{4}(\eta + \xi)^2 + \frac{\nu}{2}(\zeta_1^2 + \zeta_2^2) = \epsilon + \frac{\lambda}{4}(\eta - \xi)^2. \tag{2.11}$$

Equation (2.11) corresponds to a three-dimensional object embedded in a 4-dimensional space. Let's call *equilibrium region* $\mathcal{R}$ the one such that

$$E_l = \epsilon \qquad |\eta - \xi| < c, \tag{2.12}$$

with ϵ and c positive values. $\mathcal{R}$ is then homeomorphic to the product of a **two-sphere** and an **interval** $I = [-c; c]$. For each value in I the equilibrium region is a two-sphere: from one side it is bounded by $\eta - \xi = -c$ and from the other by $\eta - \xi = +c$.
Its projection in the $\eta - \xi$ plane is shown in Fig. 2.4. Each point in the (η, ξ) plane corresponds to a circle S^1 in $\mathcal{R}$ and the line segments $(\eta - \xi \pm c)$ represent the bounding spheres. With reference to Fig. 2.4, four types of orbits are classified:

- the origin $\eta = \xi = 0$ represents **periodic** orbits called *Lyapunov orbits*;
- **Non-transit** orbits emanate and arrive to the same bounding sphere. They correspond to the blue branches of hyperbola;
- **Transit** orbits emanate from one bounding sphere and arrive to the other. They correspond to the red branches of hyperbola;
- The line segments $\eta = 0$ or $\xi = 0$, passing through the origin, correspond to **asymptotic** orbits. They are pieces of stable and unstable manifolds separating two different kinds of motion: transit and non-transit orbits.

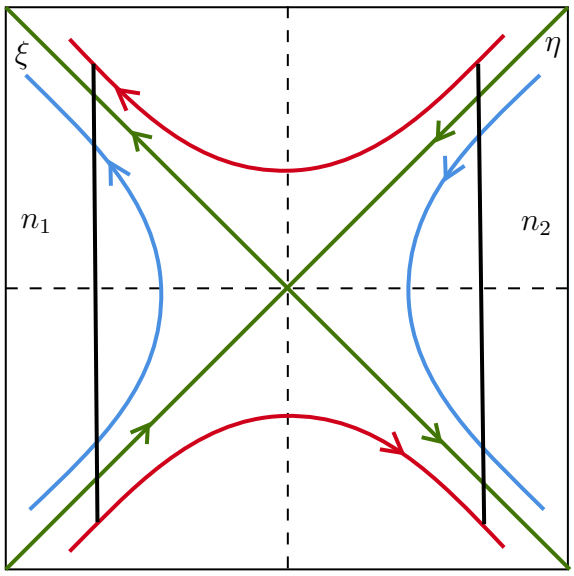

Figure 2.4: Flow in the equilibrium region - n_1 represent the bounding sphere $\eta - \xi = -c$ and n_2 corresponds to $\eta - \xi = +c$.

It is interesting to visualize these orbits in the position space, where $\mathcal{R}$ appears as the neck region connecting two realms. The general solution to the linearized system comprises - among others - two coefficients, α_1 and α_2, whose values, depending on the sign, change the type of solution obtained, as shown in Fig. 2.5.

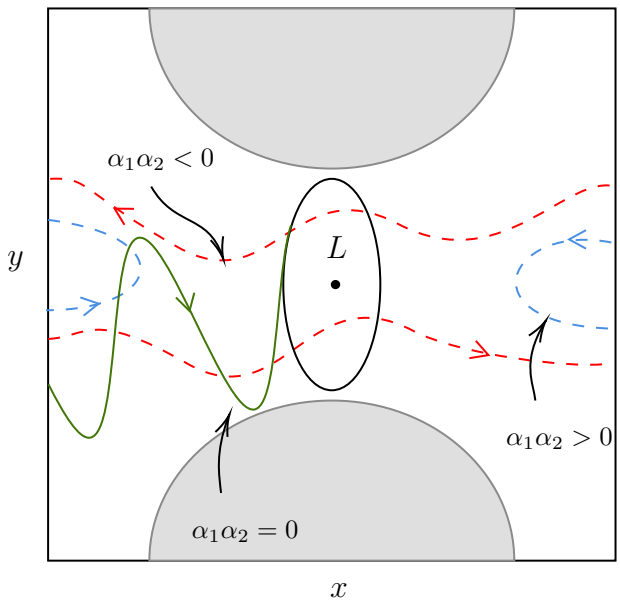

Figure 2.5: Flow in the position region.

In particular, with reference to Fig. 2.5:

- $\alpha_1 = \alpha_2 = 0$ the Lyapunov periodic orbit is obtained;
- $\alpha_1\,\alpha_2 = 0$ correspond to asymptotic orbits, marked in green;
- $\alpha_1\,\alpha_2 < 0$ correspond to transit orbits, marked in red;
- $\alpha_1\,\alpha_2 > 0$ correspond to non-transit orbits, marked in blue.

More information on the topic are available in [20].

2.1.6. Trajectory design

Space mission design is a challenging task and minimizing fuel consumption is nowadays a prerequisite for the feasibility of most missions. Before getting into the actual mission design, some mathematical tools used in this dissertation are presented.

State transition matrix

Let $\mathbf{x}$ be the six-dimensional vector composed by $\mathbf{x} = [x, y, z, \dot{x}, \dot{y}, \dot{z}]^\top$. Its variation $\delta\mathbf{x}$ can be expressed as follows $\delta\mathbf{x} = [\delta x, \delta y, \delta z, \delta\dot{x}, \delta\dot{y}, \delta\dot{z}]^\top$. The state transition matrix (STM), defined as $\mathbf{\Phi}$, relates the variation of the state at time t_0 with the variation of the state at later times t

$$\delta\mathbf{x}(t) = \mathbf{\Phi}(t, t_0)\ \delta\mathbf{x}(t_0). \tag{2.13}$$

$\mathbf{\Phi}(t, t_0)$ is a time changing matrix composed of thirty-six scalar differential equations. Its dynamics reads:

$$\dot{\mathbf{\Phi}}(t, t_0) = \boldsymbol{A}(t)\ \mathbf{\Phi}(t, t_0). \tag{2.14}$$

This set of equations represents the so-called **variational equations**. The matrix $\mathbf{A}(t)$ is the Jacobian of the system dynamics and must be evaluated along the path, therefore Eq. (2.14) must be numerically propagated with the equations of motion.

Monodromy Matrix

The monodromy matrix is simply the STM evaluated after a full period, $\mathbf{M} = \mathbf{\Phi}(T, t_0)$. It is **symplectic** since associated with an autonomous Hamiltonian system: from the property of symplectic matrices, it is known that if λ_i is an eigenvalue, then λ_i^{-1} is also an eigenvalue. Being a **real** matrix, it also possesses another feature: complex eigenvalues of real matrices always come in conjugate pairs. Additionally, $\mathbf{M}$ is associated with a periodic solution, so two unitary eigenvalues - because of the symplectic property - are always present. Finally, these eigenvalues, also known as **Floquet multipliers**, provide

information regarding the stability of the solution [16, 40]:

- $\lambda_i > 1$ is associated to an unstable solution;
- $\lambda_i < 1$ is associated to a periodic stable solution;
- $\lambda_i = 1$ no information concerning stability of the solution.

A complex eigenvalue of unit magnitude associated with a periodic orbit indicates the presence of quasi-periodic motion in its vicinity: in fact, an infinite number of quasi-periodic solutions exist as families of invariant n-dimensional tori. In the CR3BP, there is only one fundamental frequency, that is the one associated with the orbital period, so only 0- and 1-dimensional (1D) tori can be found [24].

Symmetry of the CR3BP

The equations of motion of the CR3BP exhibit two types of symmetries: for instance, **type A** requires that the trajectory passes perpendicular to the x-axis, while **type P** dictates it to pass perpendicularly to the $xz-$plane [32].
In particular,

$$\begin{aligned} \text{Type A} : (x, y, z, \dot{x}, \dot{y}, \dot{z}, t) &= (x, -y, -z, -\dot{x}, \dot{y}, \dot{z}, -t) \\ \text{Type P} : (x, y, z, \dot{x}, \dot{y}, \dot{z}, t) &= (x, -y, z, -\dot{x}, \dot{y}, -\dot{z}, -t). \end{aligned} \tag{2.15}$$

The state vectors showing symmetries of the form in Eq. (2.15) are called **mirror configurations**. Applying the **differential correction** process means propagating the trajectory from one mirror configuration until another one is reached since two mirror configurations are necessary for symmetric periodic solutions to exist [33].

Once the symmetric periodic solution and the state transition matrix are available, invariant manifolds can be computed. The STM can be evaluated at time $t = T$ to get the monodromy matrix, whose eigenvalues provide information on the stability of the solution. In particular, for the planar case, it is known that:

$$\lambda_1 > 1 \quad \lambda_2 = \frac{1}{\lambda_1} < 1 \quad \lambda_3 = \lambda_4 = 1. \tag{2.16}$$

Therefore, λ_1 corresponds to an unstable direction and λ_2 to a stable one. The eigenvectors are, respectively, $Y^u(X_0)$ and $Y^s(X_0)$, being X_0 the state at which the eigenvalues are computed. Let's also select a small displacement ϵ from X_0, whose magnitude comes from a trade-off between preserving the linearity and the integration time.

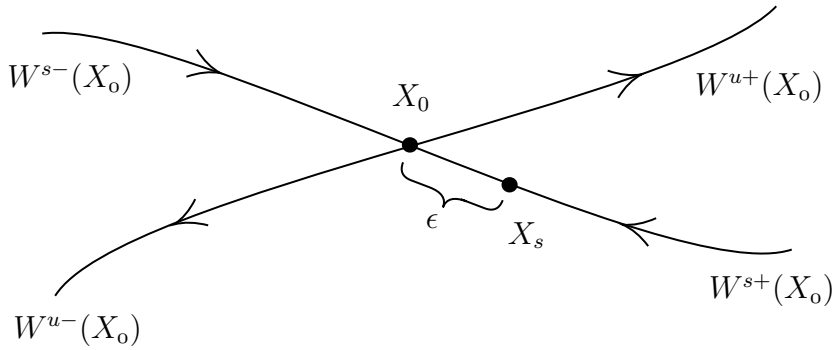

Figure 2.6: Globalization of the manifolds.

To get the full manifolds $W^{S\pm}(X_0)$ and $W^{u\pm}(X_0)$, the two vectors $X_s(X_0)$ and $X_u(X_0)$ must be integrated both forward and backward in time, in a process called *Globalization of the manifolds*:

$$\begin{aligned} X_s(X_0) &= X_0 + \epsilon\, Y^s(X_0), \\ X_u(X_0) &= X_0 + \epsilon\, Y^u(X_0), \end{aligned} \tag{2.17}$$

$W^{S\pm}(X_0)$ and $W^{u\pm}(X_0)$ correspond to the **asymptotic solutions** investigated in Section 2.1.5 if the periodic orbit under analysis is around one of the collinear equilibrium points. Especially in trajectory optimization algorithms, where the optimal manifold insertion point is sought, this procedure may represent a computational burden. Invariant manifolds can be approximated adopting a two-dimensional interpolation, followed by a nonlinear correction, so reducing the computational burden [39].

Poincaré Map

The Poincaré map is a useful tool to reduce the problem dimension, presenting the intersections between orbits in the phase space with a certain lower-dimensional subspace, transversal to the flow, called **Poincaré section**. Its importance is revealed when invariant manifolds and their intersections are used to compute orbits of desired itineraries with respect to some realms of the phase space [29]. In the case of planar systems, models are four-dimensional: using a Poincaré section, in addition to a constraint on the value of the Jacobi constant, allows a reduction in dimension such that the system is reduced to two dimensions, and the state space is completely defined through a planar projection.

Differential Correction

The **differential correction** technique, which exploits the CR3BP symmetric features, proved effective in identifying periodic solutions [17]. The integration starts at one of the

mirror configurations, i.e, $\mathbf{x}_0 = [x_0, 0, z_0, 0, y_0, 0]$ (type P) or $\mathbf{x}_0 = [x_0, 0, 0, 0, y_0, \dot{z}_0]$ (type A) and propagates to another, as the initial state $\mathbf{x}_0$ is continuously adjusted in one or more parameters, to satisfy the periodicity criteria.
For instance, if periodic solutions of type A are sought at a particular station x_0, then $\boldsymbol{\chi}_0 = [y_0, \dot{z}_0]$ represents the *free-variables* vector, containing variables that are allowed to change. The periodicity condition is then:

$$\mathbf{F}(\boldsymbol{\chi}) = \begin{bmatrix} z \\ \dot{x} \end{bmatrix}_{T/2} = \mathbf{0}. \tag{2.18}$$

In Eq. (2.18), the constraint $y_{T/2} = 0$ is not present since this condition is enforced by terminating the propagation when the solution crosses the xz-plane at $t = \frac{T}{2}$, with T the orbital period. Using Newton's method $\mathbf{F}(\boldsymbol{\chi})$ can be expanded around $\boldsymbol{\chi_0}$

$$\mathbf{F}(\boldsymbol{\chi}) = \mathbf{F}(\boldsymbol{\chi_0}) + \left.\frac{D\mathbf{F}}{D\boldsymbol{\chi}}\right|_{\boldsymbol{\chi_0}} (\boldsymbol{\chi} - \boldsymbol{\chi_0}) = \mathbf{0}. \tag{2.19}$$

From Eq. (2.19) the recursive formula can be derived:

$$\boldsymbol{\chi}_{k+1} = \boldsymbol{\chi}_k - \boldsymbol{J}(\boldsymbol{\chi}_k)^{-1}\,\mathbf{F}(\boldsymbol{\chi}_k), \tag{2.20}$$

where $\boldsymbol{J}(\boldsymbol{\chi}_k)$ is the matrix collecting the derivatives of the constraints with respect to the free variables:

$$\boldsymbol{\chi} = \begin{bmatrix} \dfrac{\partial z}{\partial y_0} & \dfrac{\partial z}{\partial \dot{z}_0} \\ \dfrac{\partial \dot{x}}{\partial y_0} & \dfrac{\partial \dot{x}}{\partial \dot{z}_0} \end{bmatrix}_{T/2} = \begin{bmatrix} \phi_{3,5} & \phi_{3,6} \\ \phi_{4,5} & \phi_{4,6} \end{bmatrix}_{T/2}, \tag{2.21}$$

where $\phi_{i,j}$ is the element (i, j) of the state transition matrix evaluated at $t = T/2$. When a good initial guess is provided, this method converges quickly to the solution. To find the next orbit in the family, a numerical **continuation** procedure is required [35].

Numerical continuation

The result of the differential correction process is the desired periodic orbit corrected within a certain tolerance. The orbit just found may be *continued*, which means that one can leverage this solution to find the next one in the family. The idea is to iteratively

vary one of the parameters while performing the differential correction. The eccentricity, mass ratio, or one of the state vector components are examples of typical parameters, here called λ. If $\mathbf{F}(\mathbf{x}_0, \lambda_0) = \mathbf{0}$ is a known solution, then the system to be solved would be:

$$\begin{cases} \mathbf{F}(\mathbf{x}, \lambda_1) = \mathbf{0}, \\ \lambda_1 = \lambda_0 + \Delta\lambda \end{cases} \tag{2.22}$$

Newton's method can be used to solve the first equality in Eq. (2.22) using as an initial guess $\mathbf{x}_0$, that, if $\Delta\lambda$ is small enough, is sufficiently close to the solution for the algorithm to converge. This procedure, known as *natural parameter continuation*, may fail when the solution branch is at a fold point because the number of solutions goes from zero to two as the parameter λ is changed. In this case, a more robust algorithm is required to recover the solution branch, such as the **pseudo arc-length continuation** [9].

2.2. Elliptic restricted three-body problem

The elliptic restricted three-body problem is the model that best describes the motion of a test particle P in a gravitational field generated by two massive bodies moving in elliptical orbits. The model is made non-dimensional by using the variable distance $d(f)$ between the primaries as the unit of length; the unit of time is chosen so that the orbital period equals 2π; the sum of the masses m_1 and m_2 gives the unit of mass [18].
The motion of P is expressed in the synodic reference frame centered at the primaries barycenter, which rotates and pulsates to keep their distance equal to one [18]. The true anomaly f replaces the time variable of the CR3BP, as illustrated in Fig. 2.7.

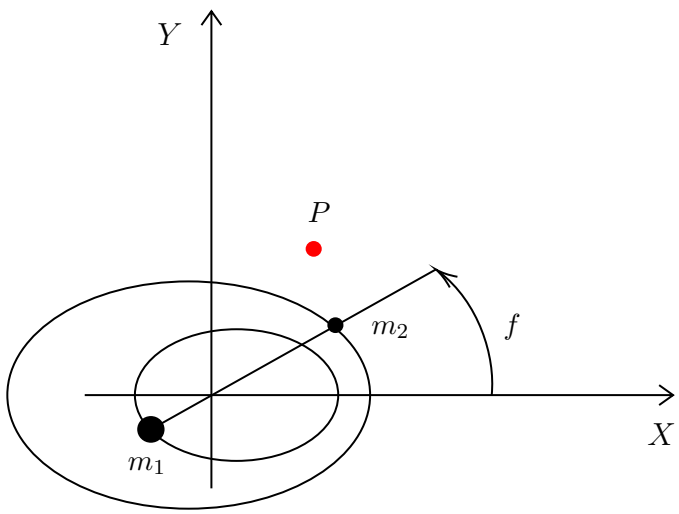

Figure 2.7: Primary and Secondary on elliptical paths.

Therefore, by designating the true anomaly f as the independent variable, the EoM of the ER3BP are given by [38]:

$$\begin{cases} x'' - 2y' = \omega_x \\ y'' + 2x' = \omega_y \\ z'' = \omega_z. \end{cases} \tag{2.23}$$

Here $(\cdot)'$ and $(\cdot)''$ denote the first and second derivative with respect to the true anomaly and $\omega_{(\cdot)}$ indicates the derivative of the potential function with respect to (.), defined as [10]

$$\omega = \frac{1}{1 + e\,\cos f}\left[\frac{1}{2}(x^2 + y^2 - z^2 e \cos f) + \frac{1-\mu}{r_1} + \frac{\mu}{r_2}\right]. \tag{2.24}$$

Unlike the CR3BP, Eqs. (2.23) are non-autonomous differential equations. For this reason, invariant manifolds are time-dependent: they are an extension to the case in which the velocity field depends on time. To identify those that have the greatest impact on the system dynamics, non-traditional techniques (for instance, variational theory of LCSs, FTLE, and Lagrangian descriptors) should be exploited.
Nevertheless, the five Lagrangian points still exist [15]. As for the circular case, a high number of studies have been devoted to the search for periodic orbits [4, 21, 31]: in the ER3BP, the entire dynamics must be replicated to have periodicity. Hence, the time-dependent positions of the primaries must also be replicated: the time dependence of the problem is due to their motion, so periodic orbits must have a period **commensurable** to that of the primaries.

2.3. Chaos Indicators

2.3.1. Finite-time Lyapunov exponents

The traditional **Lyapunov exponents** of a dynamic system give a measure of the sensitivity of the orbits of the system to the initial conditions, indicating the presence of **chaotic** dynamics. They quantify the *asymptotic* behavior of infinitesimally close particles, separated by a small distance $\delta\mathbf{Z_0}$:

$$\delta\mathbf{Z}(\mathbf{t}) = Ce^{\lambda t}\,\delta\mathbf{Z_0}, \tag{2.25}$$

If λ is positive, the distance between the particles will *asymptotically* diverge, and the system is said to be sensitive to the initial conditions. This means that even small errors in the initial conditions or some of the parameters can have a **significant impact** on the trajectory's future evolution: this is what chaos is all about, that is when the long-term prediction of a system is impossible in general [19]. This unpredictability exists at the trajectory level, which means that organizing structures that separate regions with different flow behavior can appear. The finite-time Lyapunov exponent (FTLE) field and, more specifically, its ridges have been proposed as one method for detecting these structures, also known as Lagrangian coherent structures [36].
Consider a dynamic system of the form $\dot{\mathbf{x}} = \mathbf{f}(\mathbf{x}, t)$. Its flow map $\varphi_{t_0}^{t}(\mathbf{x}_0)$ takes points from their position $\mathbf{x}_0$ at time t_0 to their position at time t. From the *gradient* of the flow map, the *Cauchy-Green strain tensor* is obtained as:

$$\mathbf{C}_{t_0}^{t_0+T} = [\nabla\varphi_{t_0}^{t}]^\top \nabla\varphi_{t_0}^{t}. \tag{2.26}$$

To compute the FTLE field from initial time t_0 to final time $t_0 + T$ at the position $\mathbf{x}_0$, one has to apply the following formula [36]:

$$\sigma_{t_0}^{T}(\mathbf{x}) = \frac{1}{|T|} \ln\sqrt{\lambda_{max}(\mathbf{C}_{t_0}^{t_0+T})}, \tag{2.27}$$

where λ_{max} is the maximum eigenvalue of the Cauchy–Green strain tensor. Equation (2.27) measures the average separation between trajectories during a specific interval of time.
Based on the definition given by Shadden et al. [36], a Lagrangian coherent structure (LCS) is the second-derivative ridge of the scalar field $\sigma_{t_0}^{T}(\mathbf{x})$. Later works revealed that, in general, observable LCSs need not be FTLE ridges, and FTLE ridges need not mark observable LCSs [13].

2.3.2. Variational theory

The variational theory was proposed by G. Haller to resolve the aforementioned inconsistencies in the theory of LCSs, due to the direct identification of the ridges of the FTLE field with Lagrangian coherent structures. Indeed, several counterexamples revealed that FTLE ridges do not mark the presence of coherent structures [13].
The variational approach aims at locating LCSs as material surfaces that pointwise extremize the **normal repulsion rate** among all close material surfaces. Let's consider a material surface $\mathcal{M}(t) \subset \mathbb{R}^n$ and an arbitrary point $\mathbf{x}_0$ that belongs to it (see Fig. 2.8).

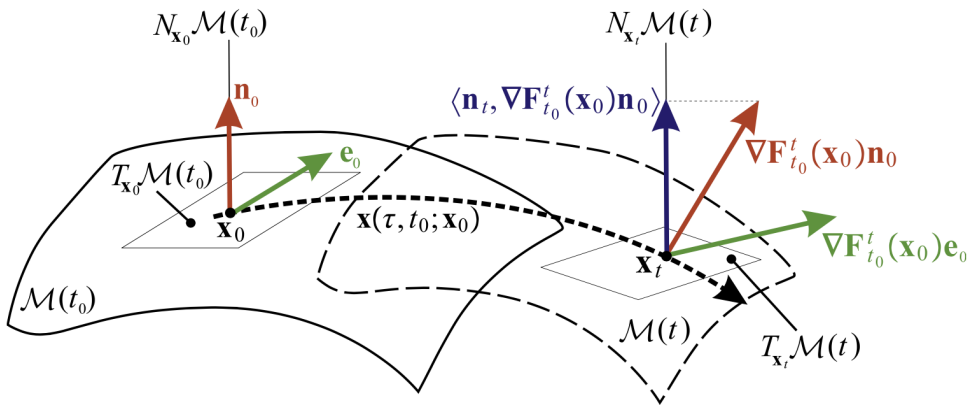

Figure 2.8: Material surface, tangent, and normal spaces; image taken from [13].

The two unitary vectors $\mathbf{e_0}$ and $\mathbf{n_0}$ are such that $\mathbf{e_0} \in T_{\mathbf{x}_0}\mathcal{M}(t_0)$ and $\mathbf{n_0} \in N_{\mathbf{x}_0}\mathcal{M}(t_0)$, i.e., the tangent space and the normal space at point $\mathbf{x}_0$, respectively. The linearized flow map, here represented as $\nabla\mathbf{F}_{t_0}^t$, carries these two vectors from time t_0 to time t. While the tangent vector $\mathbf{e_0}$ is being mapped to the tangent space $T_{\mathbf{x}_t}\mathcal{M}(t)$ due to the invariance of $\mathcal{M}(t)$ under the flow map, the normal vector $\mathbf{n_0}$ generally does not belong to $N_{\mathbf{x}_t}\mathcal{M}(t)$ but would have a general orientation [13]. As a result, to estimate the growth in the direction normal to $\mathcal{M}(t)$, the evolution of $\mathbf{n_0}$ under the flow map $\nabla\mathbf{F}_{t_0}^t(\mathbf{x}_0)\mathbf{n_0}$ must be projected onto the the unit normal vector at time t, $\mathbf{n}_t$:

$$\rho_{t_0}^t(\mathbf{x}_0, \mathbf{n}_0) = \langle \mathbf{n}_t, \nabla\mathbf{F}_{t_0}^t(\mathbf{x}_0)\mathbf{n_0} \rangle \tag{2.28}$$

$\rho_{t_0}^t(\mathbf{x}_0, \mathbf{n}_0)$ is the *normal repulsion rate*: if $\rho_{t_0}^t(\mathbf{x}_0, \mathbf{n}_0) > 1$ then $\mathcal{M}(t)$ has been overall repelling between t_0 and t. Similarly, $\rho_{t_0}^t(\mathbf{x}_0, \mathbf{n}_0) < 1$ indicates that $\mathcal{M}(t)$ has been overall attracting between t_0 and t. For this material surface to be a **repelling LCS**, its normal repulsion rate has to admit a pointwise maximum along $\mathcal{M}(t_0)$ among all sufficiently close material surfaces. The sufficient and necessary conditions for a general material surface to be a repelling LCS can be then summerized in **Theorem 1** [26].

Theorem 1 *Consider a compact material surface $\mathcal{M}(t) \subset U$ over the interval $[t_0, t_0 + T]$. $\mathcal{M}(t)$ is a repelling LCS if and only if all the following hold for all $\mathbf{x_0} \in \mathcal{M}(t)$:*

1. $\lambda_{n-1}(\mathbf{x_0}, t_0, T) \neq \lambda_n(\mathbf{x_0}, t_0, T) > 1$;
2. $\xi_{\mathbf{n}}(\mathbf{x_0}, t_0, T) \perp T_{\mathbf{x}_0}\mathcal{M}(t_0)$;
3. $\langle \nabla\lambda_n(\mathbf{x_0}, t_0, T), \xi_{\mathbf{n}}(\mathbf{x_0}, t_0, T) \rangle = 0$;
4. The Matrix $\mathbf{L}(\mathbf{x_0}, t_0, T)$, Eq. (2.29), is positive definite for all $\mathbf{x_0} \in \mathcal{M}(t)$

The first condition states that the largest eigenvalue of the Cauchy–Green tensor has to be greater than one. Moreover, its multiplicity one guarantees that the normal growth is dominant with respect to the tangential one. The second condition requires that the eigenvector $\xi_{\mathbf{n}}(\mathbf{x_0}, t_0, T)$, associated with the largest eigenvalue $\lambda_n(\mathbf{x_0}, t_0, T)$ and direction of maximum stretch, must be perpendicular to the tangent space of $\mathcal{M}(t)$. The stationary requirement for the normal repulsion rate is expressed through both the second and third conditions. Finally, the fourth condition ensures that the normal repulsion rate admits a **non-degenerate maximum** along the normal direction of $\mathcal{M}(t)$.
The Matrix $\mathbf{L}$ is given by [26]:

$$\mathbf{L} = \begin{pmatrix} \nabla^2 \mathbf{C}^{-1}[\xi_{\mathbf{n}}, \xi_{\mathbf{n}}, \xi_{\mathbf{n}}, \xi_{\mathbf{n}}] & 2\,\frac{\lambda_n - \lambda_1}{\lambda_n\,\lambda_1}\langle \xi_{\mathbf{1}}, \nabla \xi_{\mathbf{n}} \xi_{\mathbf{n}} \rangle & \dots & 2\,\frac{\lambda_n - \lambda_{n-1}}{\lambda_{n-1}\,\lambda_n}\langle \xi_{\mathbf{n-1}}, \nabla \xi_{\mathbf{n}} \xi_{\mathbf{n}} \rangle \\ 2\,\frac{\lambda_n - \lambda_1}{\lambda_n\,\lambda_1}\langle \xi_{\mathbf{1}}, \nabla \xi_{\mathbf{n}} \xi_{\mathbf{n}} \rangle & 2\,\frac{\lambda_n - \lambda_1}{\lambda_n\,\lambda_1} & \dots & 0 \\ \vdots & \vdots & \ddots & \vdots \\ 2\,\frac{\lambda_n - \lambda_{n-1}}{\lambda_{n-1}\,\lambda_n}\langle \xi_{\mathbf{n-1}}, \nabla \xi_{\mathbf{n}} \xi_{\mathbf{n}} \rangle & 0 & \dots & 2\,\frac{\lambda_n - \lambda_{n-1}}{\lambda_{n-1}\,\lambda_n} \end{pmatrix} \tag{2.29}$$

2.3.3. Lagrangian descriptors

The aim of LDs, as with FTLE ridges, and the variational theory of LCSs, is to identify phase space structures that organize the flow into different regions with different behavior. They were first introduced and applied to an altimetric ocean dataset to reveal the hidden geometry of the ocean flow [25].
To unveil these structures, this method requires the calculation of the **arc-length** of particle trajectories in a time interval $[t^* - \tau, t^* + \tau]$: if two close initial conditions are considered and their evolution during the time interval is similar, then the two arc-lengths are expected to be similar. On the other hand, if the two trajectories evolve in different ways, the arc lengths will differ: this may indicate the presence of boundaries between different regions [22].
Consider a dynamical system $\dot{\mathbf{x}} = \mathbf{v}(\mathbf{x}, t)$ with $\mathbf{x} \in \mathbb{R}^n$ and $t \in \mathbb{R}$. In its simplest case, M_1 can be obtained integrating the modulus of the velocity $\|\mathbf{v}(\mathbf{x}(t), t)\|$ starting from t^*, with $\mathbf{x}(t^*) = \mathbf{x}^*$, in the time interval $[t^* - \tau, t^* + \tau]$ [22]:

$$M_1(\mathbf{x}^*, t^*)_\tau = \int_{t^*-\tau}^{t^*+\tau} \sqrt{\sum_{i=1}^{n} \left(\frac{dx_i(t)}{\mathrm{d}t}\right)^2} \mathrm{d}t = \int_{t^*-\tau}^{t^*+\tau} \|\mathbf{v}(\mathbf{x}(t), t)\| \mathrm{d}t. \tag{2.30}$$

Families of LDs exist, depending on the integrand and on the norm adopted (See Table 2.1). Indeed, to further expand this technique, the arc-length is replaced with a geometrically or physically positive relevant quantity $|\mathcal{F}(\mathbf{x}(t))|$.

Table 2.1: Families of LDs [22].

LD	Integrand	Norm
M_1	Magnitude of velocity	L^1
M_2	Magnitude of acceleration	L^1
M_3	Magnitude of acceleration or velocity	$L^{\frac{1}{2}}$ or L^2
M_4	Magnitude of the time derivative of the acceleration	L^1
M_5	Positive quantity related to curvature	L^1

A generalization of Eq. (2.30) is provided, depending on the norm L^γ [22]:

$$\begin{aligned} &\text{If } \gamma \leq 1 \quad M(\mathbf{x}^*, t^*)_\tau = \int_{t^*-\tau}^{t^*+\tau} |\mathcal{F}(\mathbf{x}(t))|^\gamma \mathrm{d}t \\ &\text{If } \gamma > 1 \quad M(\mathbf{x}^*, t^*)_\tau = \left(\int_{t^*-\tau}^{t^*+\tau} |\mathcal{F}(\mathbf{x}(t))|^\gamma \mathrm{d}t\right)^{\frac{1}{\gamma}}, \end{aligned} \tag{2.31}$$

Although this method works successfully in various contexts [6, 8, 27, 30] it has been shown to have some **limitations** in detecting invariant manifolds in some cases [34]. Another issue is the choice of the integration time τ. Depending on its selection, one obtains different results: the organizing structures revealed by LDs generally contain more details for longer integration times. In some cases, small values of τ actually do not reveal the features associated with stable and unstable manifolds [22].

2.3.4. Qualitative trade-off

Table 2.2 shows a qualitative analysis of the chaos indicators based on the following criteria: the capability of identifying LCSs, computational efficiency, and ease of implementation. Although the variational theory is the most rigorous out of all the techniques and thus the most capable of capturing Lagrangian coherent structures, it lacks the ease of

use and computational efficiency that belong to Lagrangian descriptors. The propagation of the variational equations is required for both FTLE and variational theory but not for the LDs, making them the most computationally efficient option. The FTLE scalar field, on the other hand, is simple to implement but often ineffective at identifying LCSs, as it represents a necessary but not sufficient condition [13].
As a result of this qualitative trade-off, LDs represent the best compromise out of all the presented techniques. Consequently, they will be extensively used to study chaotic motion in the phase space for the problem at hand.

Excellent	Good	Poor	Not acceptable

	Capturing LCSs	**Comp. efficiency**	**Ease of implementation**
FTLE			
Variational theory			
LDs			

Table 2.2: Qualitative comparison of chaos indicators.

3 | Modeling of the dynamical environment

3.1. Didymos–Dimorphos binary system

In 1996, the Spacewatch project, an astronomical survey that specializes in the study of minor planets, discovered the asteroid **65803 Didymos**. More studies, seven years later, used a lightcurve analysis to confirm the presence of another body, that of its 160-metre minor-planet moon, Dimorphos. Table 3.2 outlines the physical parameters associated with the binary system, as well as the heliocentric and binary orbit characteristics.

3.2. Dynamical regimes

The dynamical environment of the Didymos-Dimorphos binary system is characterized by **low accelerations** owing to the weak and irregular gravity fields. As a result, small disturbances can induce significant changes in the dynamics of small spacecraft, especially CubeSats. Fabio Ferrari et al. [12] studied the magnitude of the accelerations acting on the Milani CubeSat as a function of the distance from the primary Didymos barycentre. For convenience, results are reported in Fig. 3.1. Close to Didymos, the gravity of the primary prevails over the solar radiation pressure (SRP) and the Sun's fourth-body effect. At approximately 10 km away, the contribution of the SRP becomes the most significant one. The Keplerian shift gradually dominates the dynamics at >1000 km from Didymos due to the Sun's fourth-body influence [12].

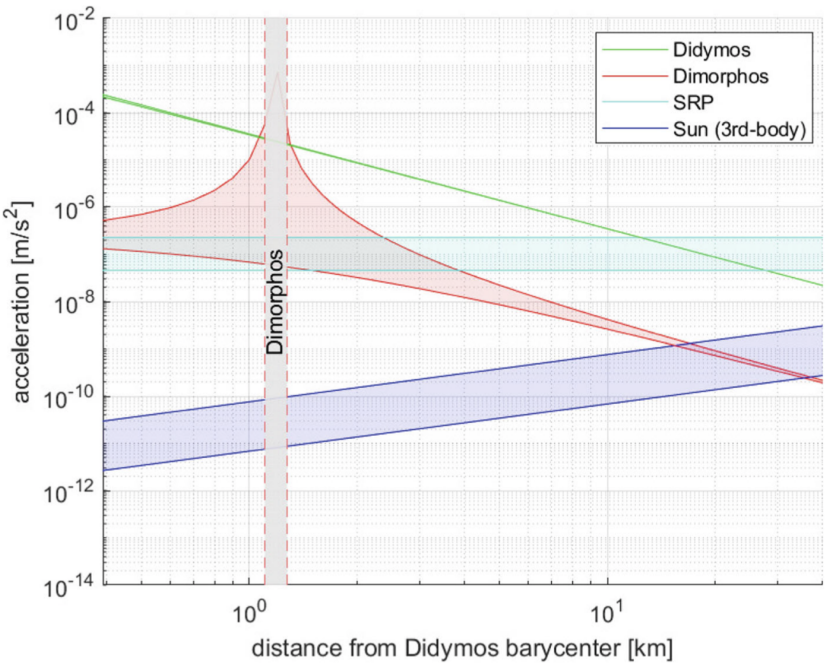

Figure 3.1: Main accelerations in the vicinity of the Didymos–Dimorphos system; image taken from [12].

3.3. Equations of motion

In the Didymos–Dimorphos chaotic environment, different contributions concur to the motion of the Spacecraft, as shown in Fig. 3.1. Consequently, the most appropriate model to describe the dynamics is the perturbed bi-elliptic restricted four-body problem (PBER4BP), which asks for the motion of a particle in a gravitational field generated by three massive bodies moving in elliptical orbits and exposed to the SRP perturbation. The following model is based on the dimensionless equations of motion of the ER3BP, with gravitational and SRP perturbations due to the Sun added to the dynamics. The non-dimensional EoM are written in a barycentric, rotating, pulsating coordinate frame, where the positions of the primaries are at rest on the x-axis. They read

$$\mathbf{r}'' + \begin{bmatrix} 0 & -2 & 0 \\ 2 & 0 & 0 \\ 0 & 0 & 0 \end{bmatrix} \mathbf{r}' = \nabla\omega + \alpha \left(\frac{\mathbf{r}_S}{\|\mathbf{r}_S\|^3} - \frac{\mathbf{r}+\mathbf{r}_S}{\|\mathbf{r}+\mathbf{r}_S\|^3} \right) + \beta \frac{\mathbf{r}+\mathbf{r}_S}{\|\mathbf{r}+\mathbf{r}_S\|^3} \tag{3.1}$$

$$\theta' = \gamma \frac{(1+e_S\cos\theta)^2}{(1-e_S^2)^{3/2}} \frac{(1-e_D^2)^{3/2}}{(1+e_D\cos f)^2} \tag{3.2}$$

The subscripts D and S in what follows refer to the binary and heliocentric orbit, respec-

tively. Equations (3.1), and (3.2) are differential equations written with respect to the true anomaly f. Perturbations due to the Sun are individually analyzed in Sections 3.3.1 and 3.3.2. The potential function ω is the same as that of the ER3BP and is given by [10]:

$$\omega = \frac{1}{1 + e_D \cos f} \left[\frac{1}{2}(x^2 + y^2 - z^2 e_D \cos f) + \frac{1-\mu}{r_{D1}} + \frac{\mu}{r_{D2}} \right] \tag{3.3}$$

Where r_{D1} and r_{D2} are the distances from the spacecraft to the primary and secondary, respectively. The two normalization factors are

$$\mathrm{TU} = \sqrt{\frac{a_D^3}{\mu_D} \frac{(1-e_D^2)^{\frac{3}{2}}}{(1+e_D \cos f)^2}}, \quad \text{and} \quad \mathrm{LU} = \frac{a_D(1-e_D^2)}{1+e_D \cos f}. \tag{3.4}$$

The parameters α, β and γ are computed as follows

$$\alpha = \frac{\mathrm{TU}^2}{\mathrm{LU}^3}\mu_S, \quad \beta = \frac{\mathrm{TU}^2}{\mathrm{LU}^3}\frac{P_0 d_{\mathrm{AU}}^2 C_r A}{m}, \quad \text{and} \quad \gamma = \sqrt{\frac{\mu_S + \mu_D}{\mu_D}\left(\frac{a_D}{a_S}\right)^3}. \tag{3.5}$$

The parameter α considers the gravitational influence of the Sun. The SRP contribution is, instead, expressed through the parameter β. In particular, the **cannonball** model was implemented for the simulations: it is, after all, the simplest and most widely used SRP model. In Eq. (3.5), C_r is the reflectivity coefficient, m is the spacecraft mass, d_{AU} is the astronomical unit, $P_0 = 4.56\,\mathrm{N\,km^{-2}}$ is the solar radiation pressure at 1 AU, A is the *projected* area, a function of the actual area illuminated by the Sun. By denoting the mass of the Sun as m_S and Didymos and Dimorphos masses as m_{D_1} and m_{D_2}, the two gravitational constants in Eqs. (3.5) are $\mu_S = G\,m_S$ and $\mu_D = G\,(m_{D1} + m_{D2})$, where G is the universal gravitational constant. The evaluation of the position vector of the Didymos–Dimorphos barycenter to the Sun indicated as $\mathbf{r}_S$ requires the knowledge of the heliocentric true anomaly θ, whose value is propagated in the EoM in Eq. (3.2). Indeed, $\mathbf{r}_S$ is computed as

$$\mathbf{r}_S = \mathbf{A}_1\,\mathbf{A}_2\,\frac{1}{\mathrm{LU}}\frac{a_S(1-e_S^2)}{(1+e_S\cos\theta)}\begin{bmatrix}\cos\theta\\ \sin\theta\\ 0\end{bmatrix}, \tag{3.6}$$

where $\mathbf{A}_2$ is the rotation matrix from the heliocentric perifocal to the ecliptic frame and $\mathbf{A}_1$ maps the rotation from the ecliptic to the rotating pulsating reference system. They

are computed as follows [7]

$$\mathbf{A}_2 = \begin{bmatrix} -s_{\Omega_S} c_{i_S} s_{\omega_S} + c_{\Omega_S} c_{\omega_S} & -s_{\Omega_S} c_{i_S} c_{\omega_S} - c_{\Omega_S} s_{\omega_S} & s_{\Omega_S} s_{i_S} \\ c_{\Omega_S} c_{i_S} s_{\omega_S} + s_{\Omega_S} c_{\omega_S} & c_{\Omega_S} c_{i_S} c_{\omega_S} - s_{\Omega_S} s_{\omega_S} & -c_{\Omega_S} s_{i_S} \\ s_{i_S} s_{\omega_S} & s_{i_S} c_{\omega_S} & c_{i_S} \end{bmatrix} \tag{3.7}$$

and [7]

$$\mathbf{A}_1 = \begin{bmatrix} c_f & s_f & 0 \\ -s_f & c_f & 0 \\ 0 & 0 & 1 \end{bmatrix} \begin{bmatrix} -s_{\Omega_D} c_{i_D} s_{\omega_D} + c_{\Omega_D} c_{\omega_D} & c_{\Omega_D} c_{i_D} s_{\omega_D} + s_{\Omega_D} c_{\omega_D} & s_{i_D} s_{\omega_D} \\ -s_{\Omega_D} c_{i_D} c_{\omega_D} - c_{\Omega_D} s_{\omega_D} & c_{\Omega_D} c_{i_D} c_{\omega_D} - s_{\Omega_D} s_{\omega_D} & s_{i_D} c_{\omega_D} \\ s_{\Omega_D} s_{i_D} & -c_{\Omega_D} s_{i_D} & c_{i_D} \end{bmatrix}, \tag{3.8}$$

in which $c_{(\cdot)}$ and $s_{(\cdot)}$ are the $\sin(\cdot)$ and $\cos(\cdot)$, respectively. The EoM were integrated in a MATLAB environment with a variable-step, variable-order Adams–Bashforth–Moulton predictor-corrector solver of orders 1 to 13 with a tolerance of 10^{-12}. Values of the parameters used for the simulations are summarized in Tables 3.1, and 3.2.

Table 3.1: Parameters cannonball model.

SRP Parameter	Symbol	**Value**	**Unit**
Spacecraft mass	m	10	kg
Projected Area	A	1.8	m^2
Reflectivity coefficient	C_r	0.2	
Astronomical unit	d_{AU}	149597870.700	km

3.3.1. Fourth-body perturbation

The Didymos–Dimorphos binary system barycentre orbits the Sun in an elliptical orbit, inclined with respect to the ecliptic. The presence of the Sun in the model requires the addition of the fourth-body acceleration to the EoM [12]:

$$\mathbf{a}_{FB} = \mu_S \left(\frac{\mathbf{r}_S}{\|\mathbf{r}_S\|^3} - \frac{\mathbf{r} + \mathbf{r}_S}{\|\mathbf{r} + \mathbf{r}_S\|^3} \right) \tag{3.9}$$

The nondimensional distance between the Didymos-Dimorpos barycenter and the Sun, $\mathbf{r}_S$, is retrieved through Eq. (3.6). To fully nondimensionalize, the parameter α in Eq. (3.5) is introduced, and Eq. (3.9) becomes:

$$\mathbf{a}_{FB}^{(\mathrm{ND})} = \alpha \left(\frac{\mathbf{r}_S}{\|\mathbf{r}_S\|^3} - \frac{\mathbf{r} + \mathbf{r}_S}{\|\mathbf{r} + \mathbf{r}_S\|^3} \right) \tag{3.10}$$

where the superscript $(\cdot)^{(\mathrm{ND})}$ means that the quantity $(\cdot)$ is dimensionless.

3.3.2. Solar radiation pressure

As shown in Fig. 3.1, the contribution of the solar radiation pressure is not marginal. If anything, it generates one of the most significant accelerations to the overall dynamics, and as such, it must be accurately predicted. Traditionally, the **cannonball** model is used for preliminary assessments in spacecraft trajectory design. The magnitude of the acceleration is given by [37]:

$$\mathbf{a}_{\mathrm{SRP}} = \frac{P_1(1 + C_r)\, A}{m} \frac{\mathbf{r} + \mathbf{r}_S}{\|\mathbf{r} + \mathbf{r}_S\|} \tag{3.11}$$

P_1 is the solar pressure, which may be computed using its value at 1 AU, P_0 :

$$P_1 = P_0 \left(\frac{d_{\mathrm{AU}}^2}{\|\mathbf{r} + \mathbf{r}_S\|^2} \right) \tag{3.12}$$

The **radiation intensity** at Earth's orbit is $S = 1367\,\mathrm{W/m^2}$, which is the energy flow transported by photons across a surface normal to the radiation direction. To determine the solar pressure P_0 at 1 AU the energy flux is divided by the speed of light c:

$$P_0 = \frac{S}{c} = 4.56 \cdot 10^{-6}\ \frac{N}{m^2}. \tag{3.13}$$

By substituting (3.12) into (3.11), $\mathbf{a}_{\mathrm{SRP}}$ becomes:

$$\mathbf{a}_{\mathrm{SRP}} = \frac{P_0 d_{\mathrm{AU}}^2 (1 + C_r) A}{m} \frac{\mathbf{r} + \mathbf{r}_S}{\|\mathbf{r} + \mathbf{r}_S\|^3}. \tag{3.14}$$

Again, the non-dimensional distance $\mathbf{r}_S$ between the Didymos–Dimorpos barycenter and the Sun is retrieved through Eq. (3.6). The parameter γ in Eq. (3.5) is introduced to fully nondimensionalize, so Eq. (3.14) becomes:

$$\mathbf{a}_{\mathrm{SRP}}^{(\mathrm{ND})} = \beta \frac{\mathbf{r} + \mathbf{r}_S}{\|\mathbf{r} + \mathbf{r}_S\|^3} \tag{3.15}$$

	Symbol	**Value**	**Unit**
Physical Parameters			
primary mass	m_{D1}	5.2294×10^{11}	kg
primary mean diameter	D_{D_1}	0.78	km
primary density	ρ_{D_1}	2170	kg/m^3
secondary mass	m_{D2}	4.8633×10^9	kg
secondary mean diameter	D_{D_2}	0.170 ± 0.030	km
secondary density	ρ_{D_2}	2170	kg/m^3
Heliocentric Orbit			
eccentricity	e_S	0.38384	
semi-major axis	a_S	1.64420	AU
inclination	i_S	3.40795	deg
longitude of the ascending node	Ω_S	73.19580	deg
argument of perihelion	ω_S	319.32295	deg
sidereal orbital period	T_S	770.07519	days
gravitational parameter	μ_S	132712439940	km^3/s^2
Binary Orbit			
eccentricity	e_D	0.03	
semi-major axis	a_D	1.19 ± 0.03	km
inclination to the ecliptic	i_D	174	deg
longitude of the ascending node	Ω_D	40	deg
argument of pericenter	ω_D	0 (assumed)	deg
secondary orbital period	T_D	11.920+0.004/-0.006	hours
ecliptic longitude	λ	310	deg
ecliptic latitude	β	-84	deg
mass ratio CR3BP	μ	0.009214	-
gravitational parameter	μ_D	$3.522\,601 \times 10^{-8}$	km^3/s^2

Table 3.2: Physical parameters of the Didymos–Dimorphos system. *Primary*: Didymos, *Secondary*: Dimorphos [12, 41].

4 | Methodology

4.1. Application of Lagrangian descriptors to astrodynamics

Lagrangian descriptors were first introduced in Section 2.3.3 as a tool for revealing phase space organizing structures in dynamical systems that depend explicitly on the independent variable t. In the bi-elliptic restricted four-body problem (BER4BP), the independent variable is no longer represented by time, but rather it is replaced by the true anomaly of the system f. For this reason, a revised version of LDs is here introduced

$$\begin{aligned} &\text{If } \gamma \leq 1 \quad M(\mathbf{x}_0, f_f) = \int_0^{f_f} |\mathcal{F}(\mathbf{x}(f))|^\gamma \mathrm{d}f \\ &\text{If } \gamma > 1 \quad M(\mathbf{x}_0, f_f) = \left(\int_0^{f_f} |\mathcal{F}(\mathbf{x}(f))|^\gamma \mathrm{d}f \right)^{\frac{1}{\gamma}} . \end{aligned} \tag{4.1}$$

The integration is carried out only for positive values of f as only the future evolution of the initial conditions (ICs) is here studied. Table 4.1 lists the family of LDs used in this work: they were numerically computed by extending the state vector $\mathbf{x} = [\mathbf{r}, \mathbf{r}']^\top$ with the selected integrand having a zero initial value. According to the heuristic argument they are based on, the LDs field divides the space of initial conditions into regions where the spacecraft motion is similar. If a stable orbit is identified in a specific region of the LD field, then every initial condition in that region will **behave similarly**.
It should be clarified that *stable* in this context refers to orbits that do not escape or impact the system for a certain amount of time.

Table 4.1: List of LDs.

LD	Integrand	Norm
M_1	$\|\mathbf{x}'\|$	L^1
M_2	$\|\mathbf{x}''\|$	L^1
M_3	$\|\mathbf{x}'\|$ or $\|\mathbf{x}''\|$	$L^{\frac{1}{2}}$ or L^2
M_4	$\|\mathbf{x}'''\|$	L^1
M_5	Positive quantity related to curvature	L^1
M_v	$\|\sqrt{x'^2 + y'^2 + z'^2}\|$	L^1
M_a	$\|\sqrt{x''^2 + y''^2 + z''^2}\|$	L^1

4.2. Finding regions of bounded motion

The process of finding bounded orbits about Dimorphos is made of two stages:

1. classification of the regions of the LD field through spatial resonant periodic solutions in the simplified, autonomous CR3BP starting from a planar family of distant retrograde orbits (DROs);
2. computation of the LD field within more representative, non-autonomous dynamical models, and phase space sampling to find bounded orbits.

Stage 1 is intended to educate the method about the location of bounded and unbounded regions of motion. Indeed, the behavior of the discovered areas of the LD field is, a priori, unknown. To this purpose, initial conditions of DROs were inspected against the LD field in the planar CR3BP: as they are bounded orbits, their ICs are expected to lie within regions of stable motion. This procedure is repeated for the spatial problem, with the ICs of spatial resonant periodic orbits acting as identifiers.
In stage 2, the LD field is computed within non-autonomous models of increasing degree of fidelity, and the phase space is sampled to find bounded orbits. These models are examined **one at a time**: first, the ER3BP. Second, the Sun's presence is considered in the BER4BP, and, eventually, the SRP perturbed BER4BP.
The LD field is expected to evolve as the fidelity and complexity of the system are increased. Regions of stable motion found in stage 1 may appear stretched and compressed into small regions or even disappear, while large regions of unstable motion take over. If stable regions still exist, then bounded orbits are expected to be inside of them.

4.3. Periodic orbit research

4.3.1. Distant retrograde orbits

DROs are a class of orbits obtained from the analysis of simple-periodic symmetrical orbits in Hill's limiting case of the restricted three-body problem, i.e., when the mass of the secondary tends to zero [14]. DROs exhibit **retrograde motion**, as opposed to the rotation of the secondary around the primary [3].
This class of orbits may be generated in the CR3BP ($\alpha = 0$, $\beta = 0$, $e_D = 0$ in Eq. (3.1)) by starting from a mirror configuration $\mathbf{x_0} = [x_0, 0, 0, 0, \dot{y}_0, 0]$ and applying **differential correction** and **numerical continuation** procedures.

Differential correction

The integration starts from a mirror configuration and terminates once the trajectory crosses the xz-plane. For the orbit to be symmetric, the orbital state at the crossing, occurring at $t = \frac{T}{2}$ where T is the orbital period, should be $\mathbf{x_1} = [x_1, 0, 0, 0, \dot{y}_1, 0]$. The *free variable* is $\chi = \dot{y}_0$, and the constraint is specified as $F(\chi) = \dot{x}_1 = 0$, while the condition $y_1 = 0$ is automatically enforced by stopping the integrator at the crossing. The recursive formula can be derived through Newton's method as:

$$\dot{y}_0^{(k+1)} = \dot{y}_0^{(k)} - \left(\phi_{4,5}^{(k)}\right)^{-1} \dot{x}_{T/2}^{(k)} \tag{4.2}$$

If the initial guess is appropriate, the algorithm usually converges to $F(\chi) < \epsilon = 10^{-12}$ after a few iterations. A continuation procedure is then required to find more periodic orbits in the family.

Numerical continuation

The numerical continuation procedure uses as a natural parameter the initial station x_0. Let $\mathbf{x_0} = [x_0, 0, 0, 0, \dot{y}_0, 0]$ be the outcome of the differential correction process, that is, a periodic orbit corrected within a certain tolerance. To find the next orbit in the family, the natural parameter is slightly increased to x_1, while the value of $\dot{y}_0$ is retained. The new initial guess is then $\mathbf{x_1} = [x_1, 0, 0, 0, \dot{y}_0, 0]$, and the differential correction process is iteratively repeated. The full algorithm can be outlined as follows:

Algorithm 4.1 Building of DROs family

```
for i = 1 to i= N_family do
    while |ẋ_{T/2}| < ϵ,  K < K_max do
        Integrate till xz-plane crossing
        Apply recursive formula                    ▷ Differential correction
    end while
    Store ẏ_0 for continuation
    if |ẋ_{T/2}| < ϵ then                          ▷ If a solution is found
        Increment x_0                              ▷ Continuation
        Build new initial guess
    end if
end for
```

where N_{family} is the number of DROs to be computed and K_{max} provides an exit condition in case of failure.

4.3.2. Spatial resonant periodic orbits

Spatial resonant periodic orbits in the CR3BP are based on vertical bifurcations from a family of planar periodic solutions [5]. The monodromy matrix plays a key role in determining resonant orbits, and it is calculated for each DRO. Indeed, let's denote as λ_i and λ_j the two complex conjugate eigenvalues and as $\{\mathbf{e}_i, \mathbf{e}_j\}$ the corresponding eigenvectors. As the system is Hamiltonian, the relationship $\lambda_i \cdot \lambda_j$ holds for each pair of eigenvalues and, therefore, they can be written as $\lambda_i = \cos(\theta) + i\sin(\theta)$ and $\lambda_j = \cos(\theta) - i\sin(\theta)$, where i is the imaginary unit. An infinitesimal displacement in the span $\{\mathbf{e}_i, \mathbf{e}_j\}$ will rotate by an angle θ per period [5]. The construction of a spatial orbit with a specific resonance requires the fulfillment of two conditions:

1. the two eigenvectors $\{\mathbf{e}_i, \mathbf{e}_j\}$ must have components both in the z and $\dot{z}$ directions;
2. the accumulated phase difference after n revolutions on the reference orbit should be $n\theta = 2k\pi$, where n and k are positive integers.

The value of θ can be inferred from λ_i, in particular:

$$\begin{aligned}
\left(\lambda_i + \frac{1}{\lambda_i}\right)\frac{1}{2} &= \left(\cos\theta + i\sin\theta + \frac{1}{\cos\theta + i\sin\theta}\right)\frac{1}{2} \\
&= \left(\cos\theta + i\sin\theta + \frac{\cos\theta - i\sin\theta}{\cos\theta - i\sin\theta}\cdot\frac{1}{\cos\theta + i\sin\theta}\right)\frac{1}{2} \\
&= (\cos\theta + i\sin\theta + \cos\theta - i\sin\theta)\frac{1}{2} \\
&= \cos\theta
\end{aligned} \tag{4.3}$$

Finally, the value of θ is:

$$\theta = \arccos\left[\left(\lambda_i + \frac{1}{\lambda_i}\right)\frac{1}{2}\right]. \tag{4.4}$$

The relation $n\theta = 2k\pi$ may be rewritten as:

$$n = \frac{2\,k\,\pi}{\arccos\left[\left(\lambda_i + \frac{1}{\lambda_i}\right)\frac{1}{2}\right]}. \tag{4.5}$$

Positive integers of n and k can be determined for each DRO, resulting in a different resonance for each planar periodic solution. If the eigenvectors form a span in the z and $\dot{z}$ directions, the vertical family of multiplicity[1] n intersects with the generating family. Once the values of n/k are determined, the differential correction and numerical continuation procedures can be applied.

Differential correction

In contrast to the DROs case, the integration starts at the mirror configuration $\mathbf{x}_0 = [x_0,\, 0,\, z_0,\, 0,\, \dot{y}_0,\, 0]$ and stops when the trajectory crosses the xz-plane for the n-th time. At that crossing, $t = \frac{T}{2}$. The initial values of x_0 and $\dot{y}_0$ are obtained from the 2D DROs, while z_0 must be sufficiently small for $\mathbf{x}_0$ to be an appropriate initial guess.
By selecting as free variables vector $\chi = [x_0,\, \dot{y}_0]$ and as constraints vector $F(\chi) = [\dot{x}_0,\, \dot{z}_0]$, the recursive formula reads:

$$\begin{bmatrix} x_0 \\ \dot{y}_0 \end{bmatrix}^{(k+1)} = \begin{bmatrix} x_0 \\ \dot{y}_0 \end{bmatrix}^{(k)} - \begin{bmatrix} \phi_{4,1} & \phi_{4,5} \\ \phi_{6,1} & \phi_{6,5} \end{bmatrix}^{(k)} \begin{bmatrix} \dot{x}_0 \\ \dot{z}_0 \end{bmatrix}^{(k)}. \tag{4.6}$$

As before, a continuation procedure is required to find the next orbits in the family.

Numerical continuation

The numerical continuation procedure uses as a natural parameter the initial position on the z-axis z_0, resulting in orbits with increasing z-amplitude. To find the next orbit in the family, the natural parameter is slightly updated while the values of x_0 and $\dot{y}_0$ are retained. The full algorithm can be outlined as follows:

[1] The *multiplicity* of a periodic orbit is defined as the number of consecutive intersections with the plane $y = 0$ in the same direction during one period.

Algorithm 4.2 Building of periodic spatial resonant orbits

```
for i = 1 to i= N_family do
    while |ẋ_{T/2}| < ε,  |ż_{T/2}| < ε,  K < K_max do
        Integrate till the n-th xz-plane crossing
        Apply recursive formula                          ▷ Differential correction
    end while
    Store x_0 for continuation
    Store ẏ_0 for continuation
    if |ẋ_{T/2}| < ε,  |ż_{T/2}| < ε,  then             ▷ If a solution is found
        Increment z_0
        Build new initial guess                          ▷ Continuation
    end if
end for
```

where N_{family} is the number of resonant orbits to be computed and K_{max} provides an exit condition in case of failure.

5 Results

5.1. Investigation in the circular restricted three-body problem

The LDs scalar fields for the planar problem are calculated on the Poincaré section $y = \dot{x} = 0$ ($x^{'} = 0$ for the elliptic case), using a grid enclosing the span of the DROs' ICs. The number of points (ICs) used for grid generations depends upon the final purpose. In particular, a small number of ICs is used for investigations on the capability of the different LDs in revealing organizing structures and on the effect of the final true anomaly. Conversely, an elevated number of points is used for the phase space sampling since higher resolutions let smaller structures emerge. Finally, the grid width is equal for all the simulations: when the system is two-dimensional, only the parameters x_0 and $\dot{y}_0$ (${y_0}^{'} = 0$ for the elliptic case) are considered (See Table 5.1).

Table 5.1: Grid width. The parameters are expressed in the nondimensional reference system.

Parameter	**Lower Bound**	**Upper Bound**
x_0	0.75	0.95
$\dot{y}_0$, $y_0^{'}$	0.328296	0.6045280
z_0	0	0.03

5.1.1. Lagrangian descriptors comparison

All the LDs listed in Table 4.1 are used, but only the more capable one in giving insightful dynamical information is retained. In order to compare them, the different LDs are computed in the planar CR3BP for a final true anomaly of $f_f = 5\pi$; they are shown for comparison in Fig. 5.1, on a grid of 200×200 ICs.

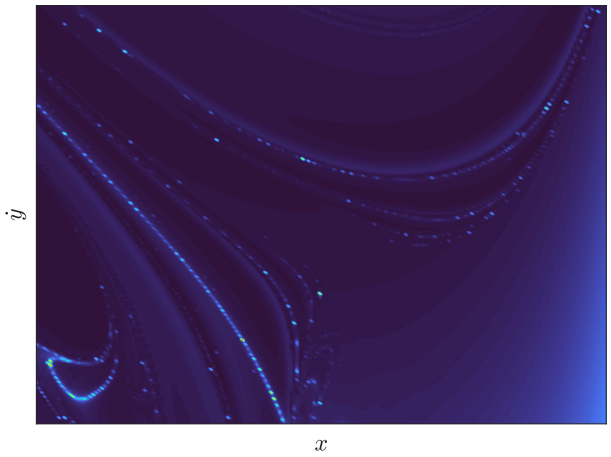

(a) M_1, $f_f = 5\pi$.

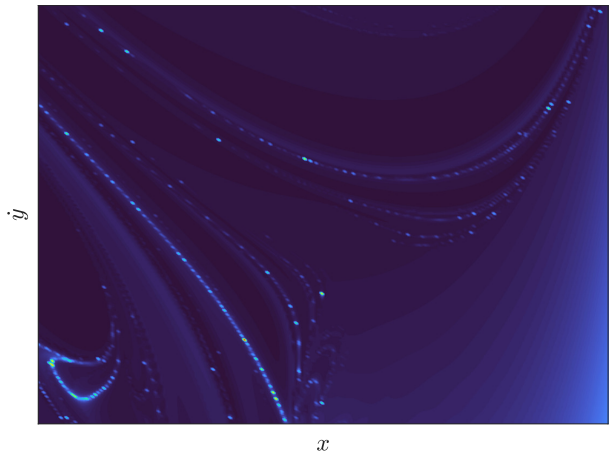

(b) M_2, $f_f = 5\pi$.

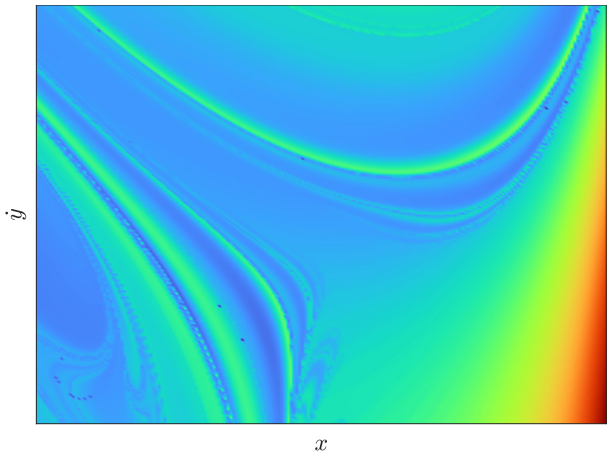

(c) M_3, $f_f = 5\pi$.

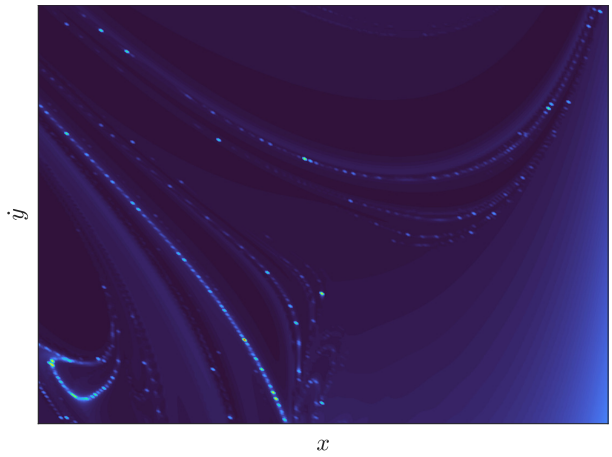

(d) M_4, $f_f = 5\pi$.

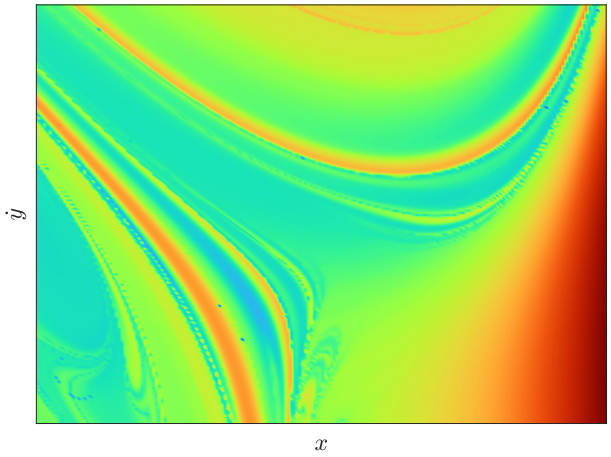

(e) M_5, $f_f = 5\pi$.

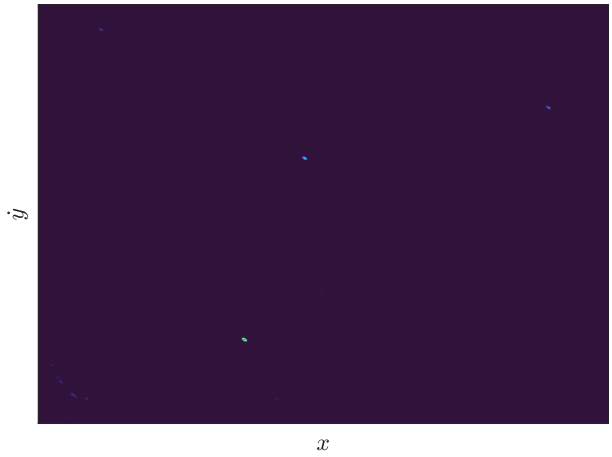

(f) M_a, $f_f = 5\pi$.

Figure 5.1: LD in comparison for a $f_f = 5\pi$.

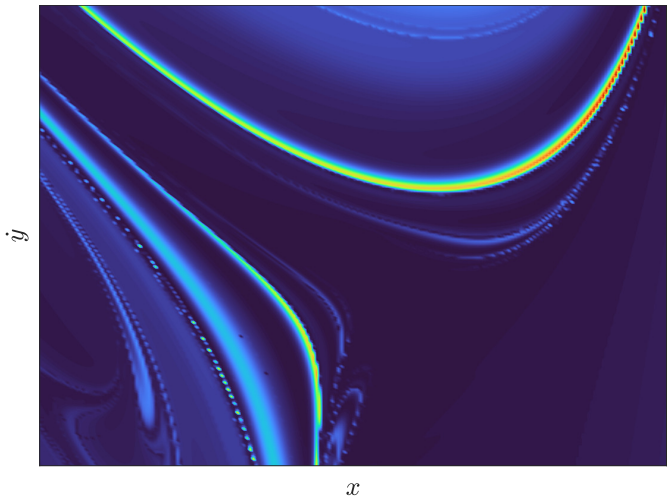

(g) M_v, $f_f = 5\pi$.

Figure 5.1: LD in comparison for a $f_f = 5\pi$.

Almost all of the LDs proved to be effective in revealing phase space structures. In fact, they unveil the same dynamical patterns at different scales. M_a, on the other hand, seems not to catch enough dynamical information. The Lagrangian descriptors M_1 and M_v are the most computationally efficient options since they require only the evaluation of the state derivative. Conversely, other LDs demand the evaluation of higher-order derivatives. As a result, M_1 and M_v are temporarily selected: only the one showing more features for longer integration time will be kept.

5.1.2. Final true anomaly dependence

The selection of the final true anomaly depends on the problem at hand. In general, short integration times do not reveal a clear distinction among regions with different dynamics. Similar trajectories evolution for small values of f_f can highly diverge in the future, that is, for a higher value of the final true anomaly. Three different choices of f_f, namely 5π, 10π, and 20π, are compared to select the value that results in richer dynamical information while preserving a reasonable integration time. Once again, the underlying dynamics is the planar CR3BP. Results are shown in Fig. 5.2.

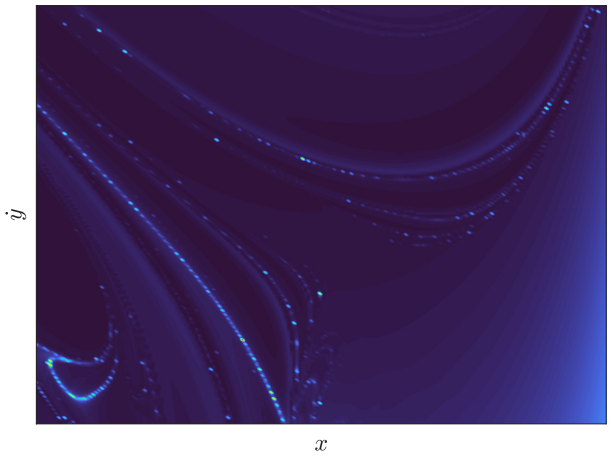

(a) M_1, $f_f = 5\pi$.

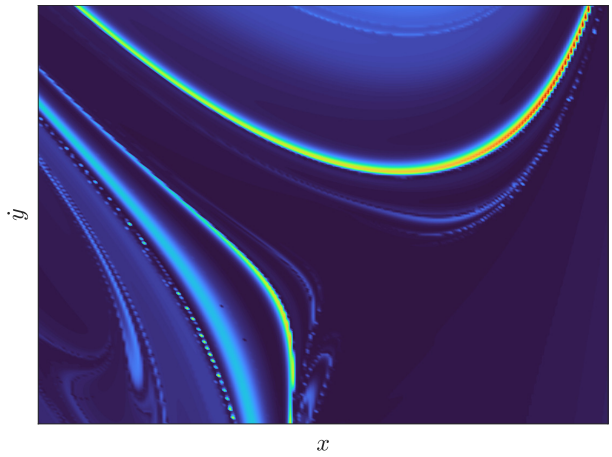

(b) M_v, $f_f = 5\pi$.

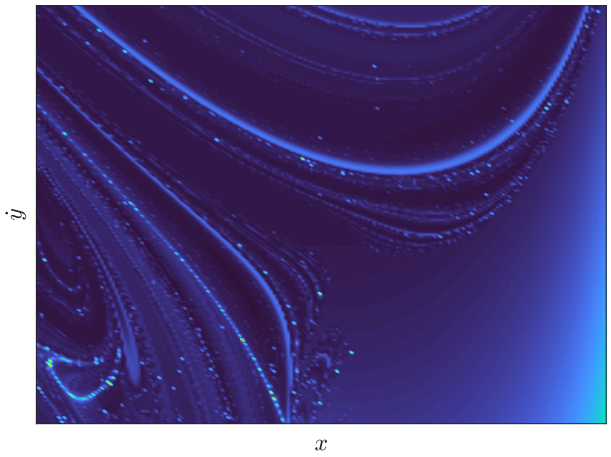

(c) M_1, $f_f = 10\pi$.

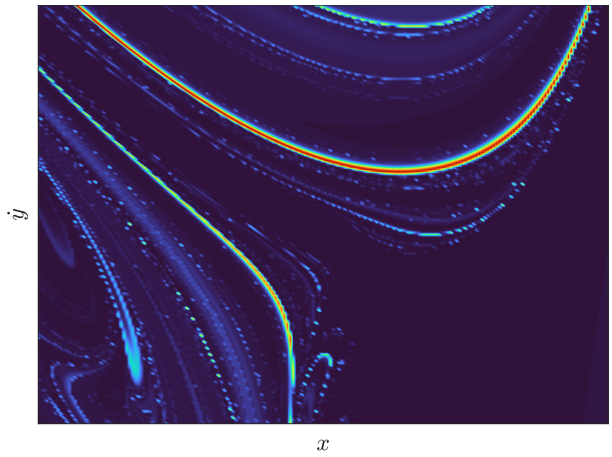

(d) M_v, $f_f = 10\pi$.

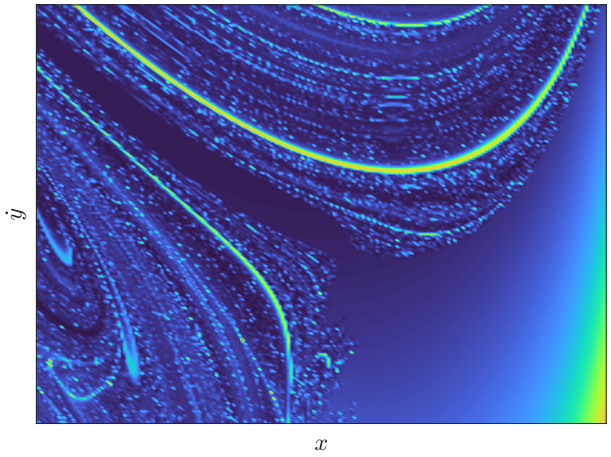

(e) M_1, $f_f = 20\pi$.

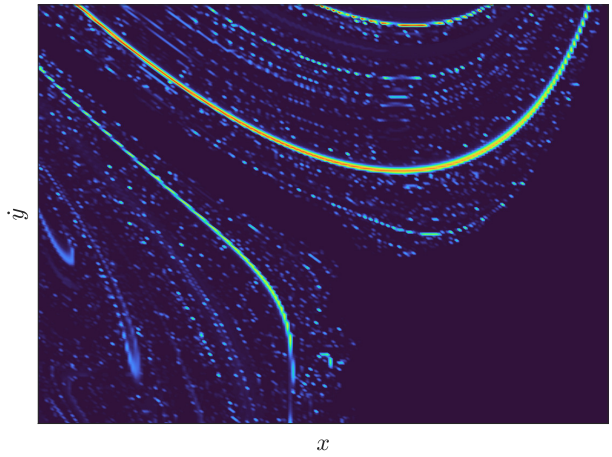

(f) M_v, $f_f = 20\pi$.

Figure 5.2: M_1 and M_v in comparison for different values of f_f.

Starting from the lowest value, it appears that increasing the value of f_f causes the dynamical structures to evolve and mature into smooth areas isolated by many separatrices: this comes at the expense of longer integration times, which are still manageable.
The final selection is then dictated by the longest integration time $f_f = 20\pi$, that is, ten revolutions of the primaries. Although in the first two cases ($f_f = 5\pi$ and $f_f = 10\pi$) M_v brings out sharper separatrices, M_1 outperforms M_v for the selected integration span: it exhibits more features associated with the different regions of motion. Accordingly, M_1 will be used for the rest of the work.

5.1.3. Classification of regions in the planar case

One hundred DROs revolving about Dimorphos are computed in the planar circular restricted three-body problem (PCR3BP) in the nondimensional span $x_0 \in [0.8, 0.9]$, with a distance among them of $\Delta x_0 = 10^{-3}$. Figure 5.3 shows the family of DROs, which will act as an identifier for the regions of the 2D LD field.

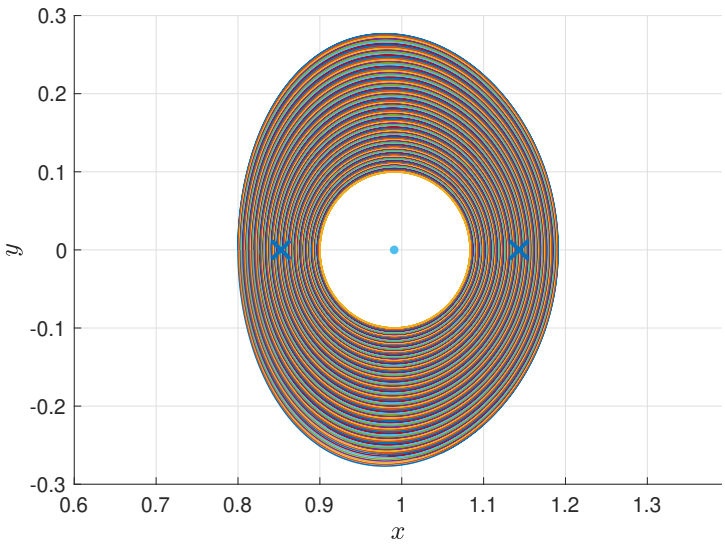

Figure 5.3: Family of DROs. The blue dot represents Dimorphos. The two blue crosses are the Lagrangian points L_1 and L_2.

The set of ICs of the 2D DROs is inspected against the LD scalar field in Fig. 5.4, to classify the regions of bounded and unbounded motion.

The red curve represents the set of DROs' ICs, and it lies in the smooth region that extends from the bottom-right to the top-left of the graph, narrowing as velocity and distance from Dimorpohos increase. The smooth region is then thought to contain ICs that persistently

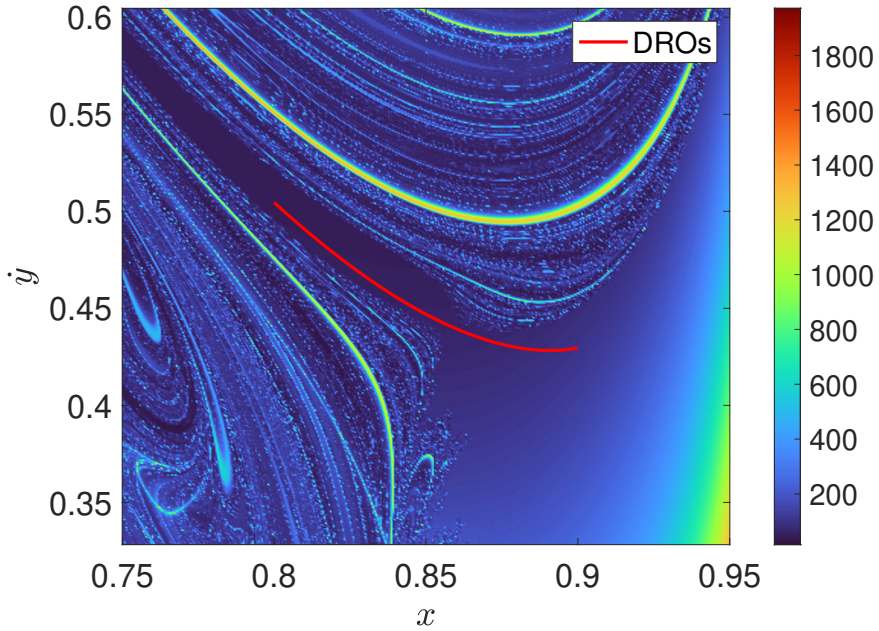

Figure 5.4: M_1 scalar field. The red curve is the Family of DROs.

revolve about Dimorphos. On its sides, on the other hand, chaotic regions appear: they are well-separated from the smooth region and are expected to contain only unbounded orbits.

The smooth region is at the **core** of this investigation: the aim is to track how it changes as more representative models are used; if it still exists, then bounded solutions are expected not to vanish.

5.1.4. Classification of regions in the three-dimensional case

The three-dimensional resonant periodic solutions are built by studying the vertical bifurcations of the family of planar DROs [23]. The study of vertical bifurcations requires the monodromy matrix, whose eigenvalues and eigenvectors provide information regarding periodic solutions in the vicinity of the reference orbit. In particular, eigenvectors having components in the z and $\dot{z}$ directions are used to obtain the resonance ratios n/k, through Eq. (4.5). The result is shown in Fig. 5.5, as a function of the dimensionless x coordinate.

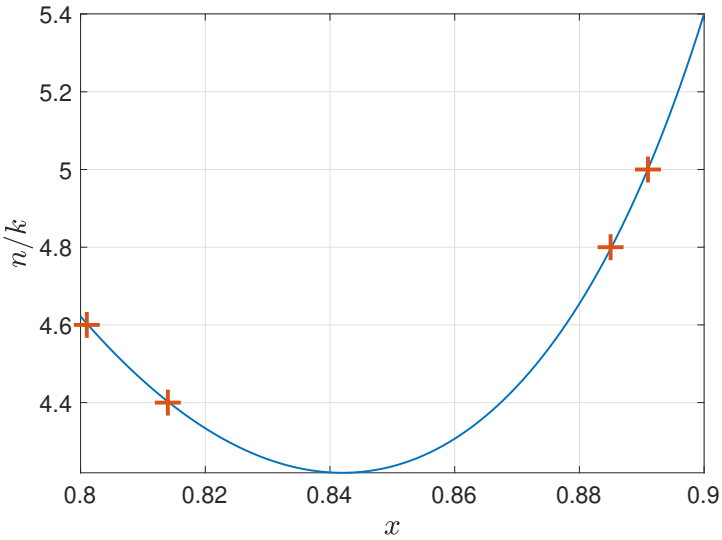

Figure 5.5: n/k as a function of the dimensionless x coordinate. The four red crosses represent the selected ratios.

The four red crosses illustrate the values n/k chosen to continue the 2D family: these ratios are selected to be rational numbers, so as to have integers of n and k. Table 5.2 lists the resonances along with the corresponding x and $\dot{y}$ coordinates.

Table 5.2: Resonances selected to continue the 2D family of DROs.

x	$\dot{\mathbf{y}}$	**n/k**	**n**	**k**
0.814	0.485515	4.4	22	5
0.8	0.504528	4.6	23	5
0.885	0.428743	4.8	24	5
0.891	0.469735	5	5	1

The resonance of the corresponding spatial periodic orbits is $(n-k):n$, where $n-k$ denotes the number of vertical revolutions [5]. The techniques of differential correction and numerical continuation can now be applied using as initial guesses the x and $\dot{y}$ values listed in Table 5.2. The continuation parameter is the dimensionless z component, whose value is progressively increased with a $\Delta z = 10^{-3}$, from $z = 0$ to $z = 0.03$.
The orbits with the highest z component are shown in Fig. 5.6.

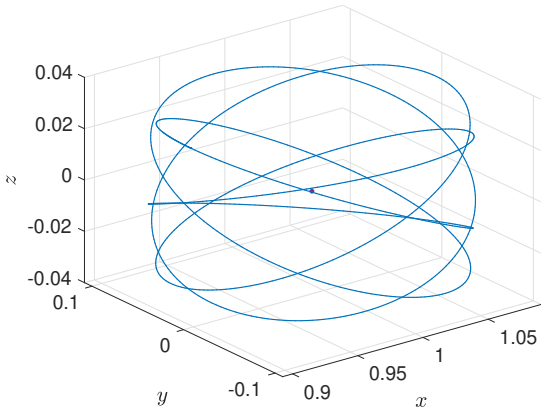

(a) $n/k = 5$

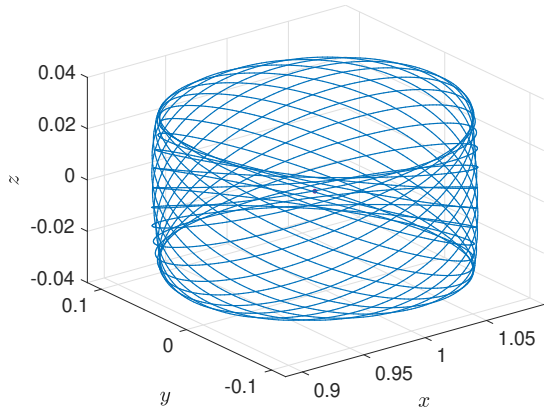

(b) $n/k = 4.8$

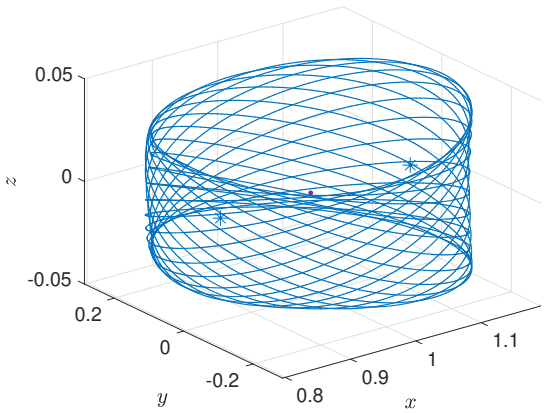

(c) $n/k = 4.6$

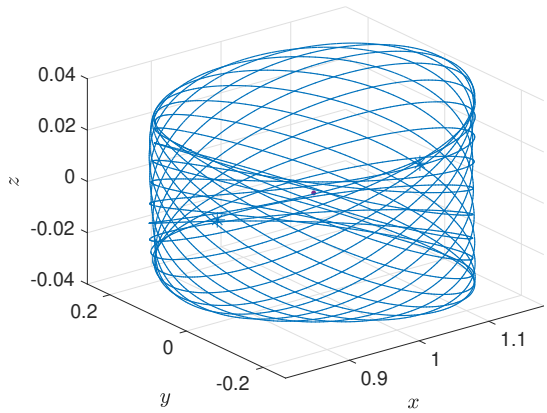

(d) $n/k = 4.4$

Figure 5.6: Resonant orbits around Dimorphos with $z = 0.03$, for different values of n/k. For a better orbits representation, data units are not the same along each axis.

5.2. Bounded orbits through phase space sampling

The second stage in the search for bounded orbits about Dimorphos plans to sample the phase space, progressively considering an increasing degree of model fidelity. Moreover, Didymos and Dimorphos are considered to be point masses, and physical collisions with them are not checked. The grid width is the same for all the simulations (see Table 5.1), as well as the final true anomaly of $f_f = 20\pi$. As the grid is three-dimensional, the evolution of the LD field is first observed at different non-dimensional z slices. The highest–z slice of the scalar field is afterward sampled to search for bounded orbits that could potentially map the whole surface of Dimorphos. The implemented grid consists of $400 \times 400 \times 5$

points along x,y, and z, respectively.

5.2.1. Sampling in the circular restricted three-body problem

The evolution of the LD field in the circular restricted three-body problem is shown in Fig. 5.7: the same pattern is repeated over different z slices, suggesting that bounded out-of-plane orbits exist. The four red lines extending from $z = 0$ to $z = 0.03$ are the resonant orbits ICs, intersecting the different slices always in the smooth area, preserving its one-to-one correspondence with bounded motion.

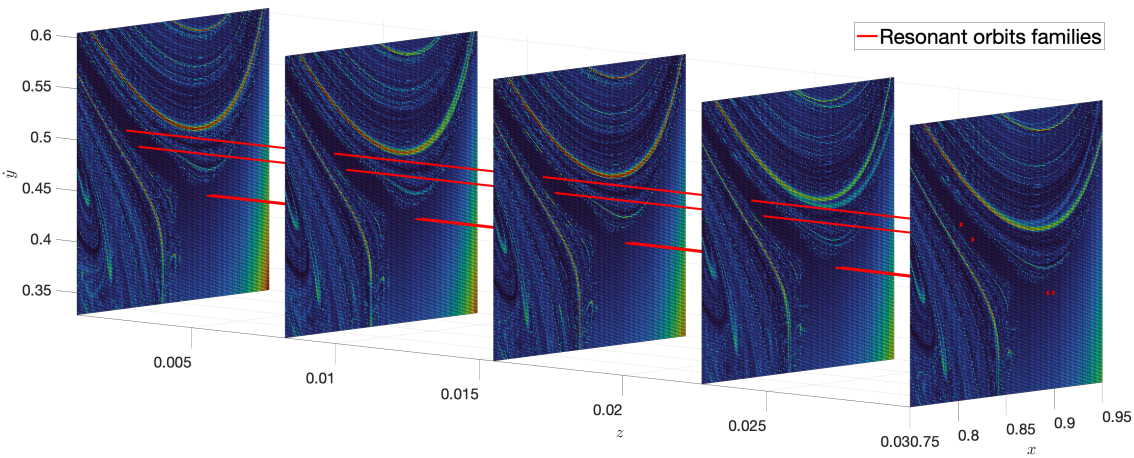

Figure 5.7: LD M_1 in the CR3BP at different z slices.

Without any loss of generality, the analysis is now restricted to the highest-z slice ($z = 0.03$) of the LD field. Five sample points are picked at different locations of the LD field, and the behavior of the resulting orbits is investigated in Fig. 5.8.
Three sample points are picked in the smooth area, while the remaining two are enclosed within the chaotic ones. The first three points (A, B, and E) exhibit bounded motion by behaving similarly to the family of resonant orbits previously found, while the other two (C and D) immediately escape the system.

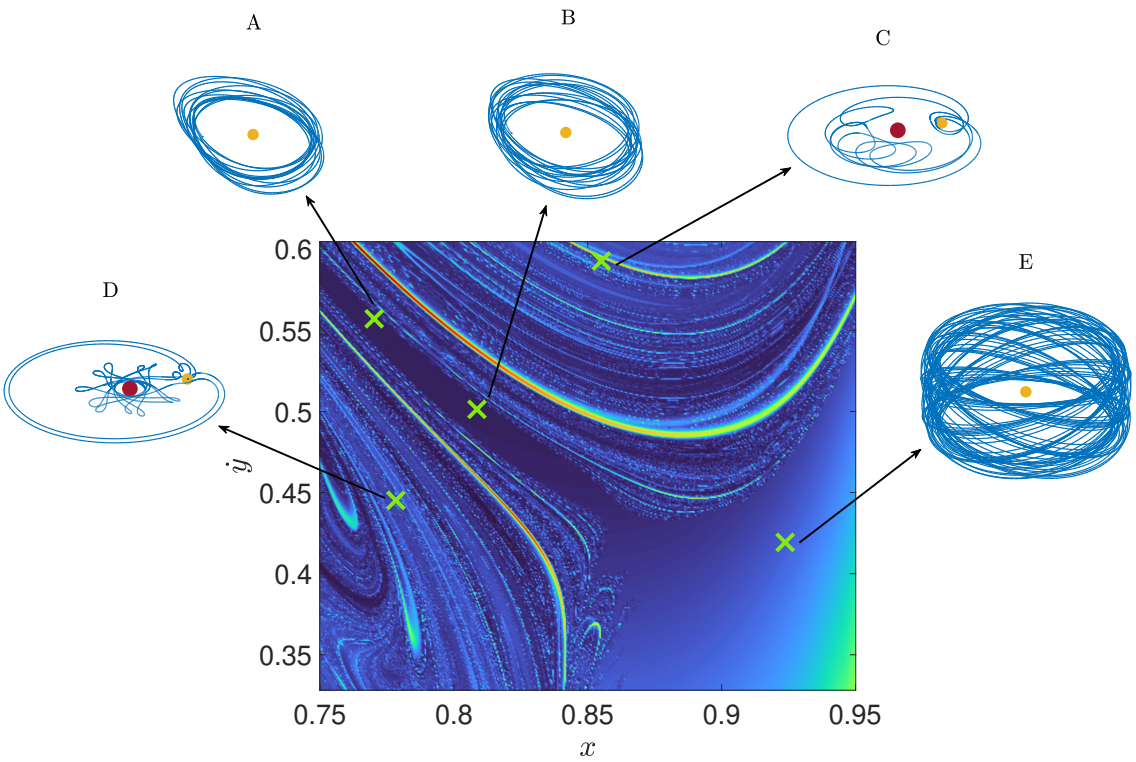

Figure 5.8: M_1 sampling in the CR3BP. The red and yellow dots are Didymos and Dimorphos not to scale, respectively.

Their ICs are listed in Table 5.3, and the trajectories are shown in the three different projections in Fig. 5.9.

Table 5.3: Orbits ICs in the CR3BP.

Orbit	$\mathbf{x}_0$	$\mathbf{y}_0$	$\mathbf{z}_0$	$\dot{\mathbf{x}}_0$	$\dot{\mathbf{y}}_0$	$\dot{\mathbf{z}}_0$	**Motion**
A	0.770202	0	0.03	0	0.557094	0	Bounded
B	0.808585	0	0.03	0	0.501289	0	Bounded
C	0.855050	0	0.03	0	0.592727	0	Escape
D	0.778282	0	0.03	0	0.445167	0	Escape
E	0.923737	0	0.03	0	0.419280	0	Bounded

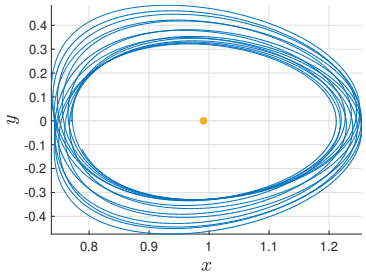

(a) A: xy-plane.

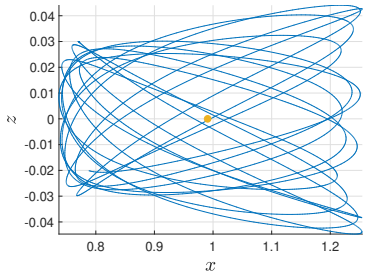

(b) A: xz-plane.

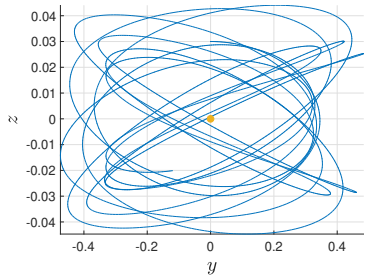

(c) A: yz-plane.

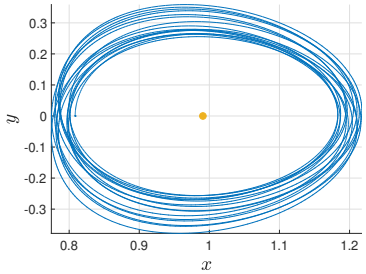

(d) B: xy-plane.

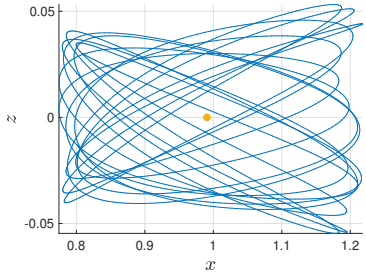

(e) B: xz-plane.

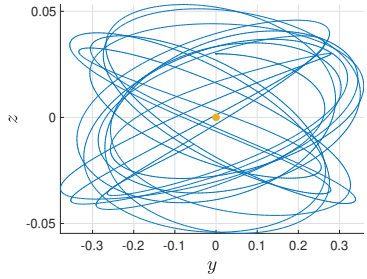

(f) B: yz-plane.

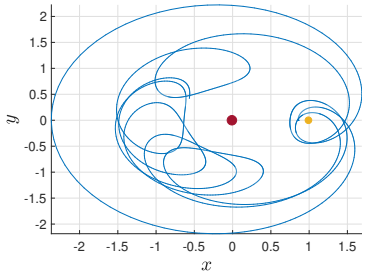

(g) C: xy-plane.

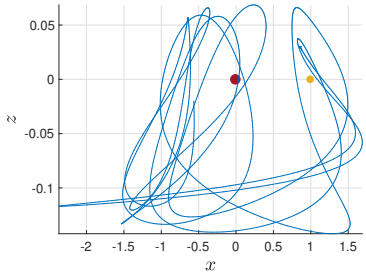

(h) C: xz-plane.

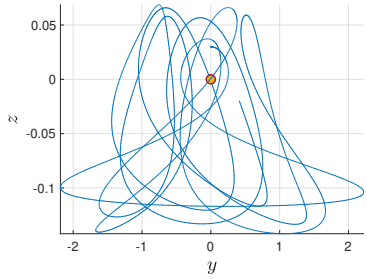

(i) C: yz-plane.

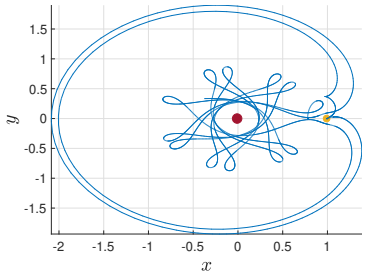

(j) D: xy-plane.

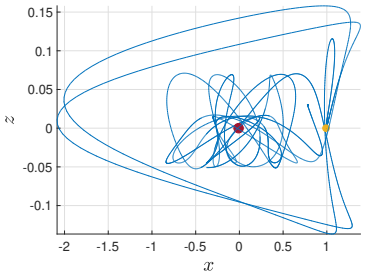

(k) D: xz-plane.

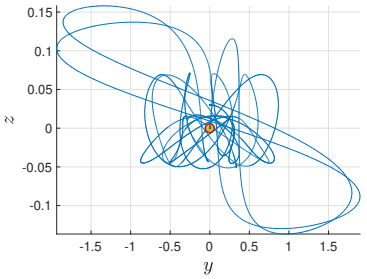

(l) D: yz-plane.

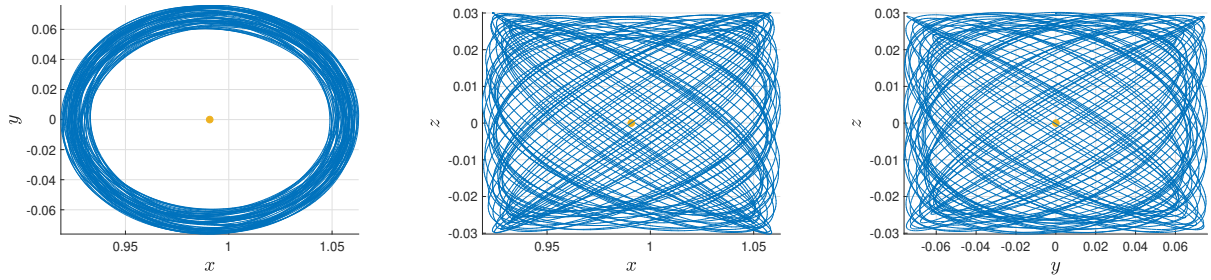

(m) E: xy-plane. (n) E: xz-plane. (o) E: yz-plane.

Figure 5.9: Samples evolution in the CR3BP. The red and yellow dots are Didymos and Dimorphos not to scale, respectively. For a better orbits representation, data units are not the same along each axis.

5.2.2. Sampling in the elliptic restricted three-body problem

The small ellipticity of the binary orbit is considered in the ER3BP ($\alpha = 0$, $\beta = 0$ in Eq. (3.1)): its value is $e_D \approx 0.03$ and, therefore, the LD field is expected to undergo minor modifications with respect to the case of circular orbits, maintaining the same structures already found. The evolution at different z is shown in Fig. 5.10: the LD field subtly changes as z increases, leading the way to a whole region of possible out-of-plane orbits.

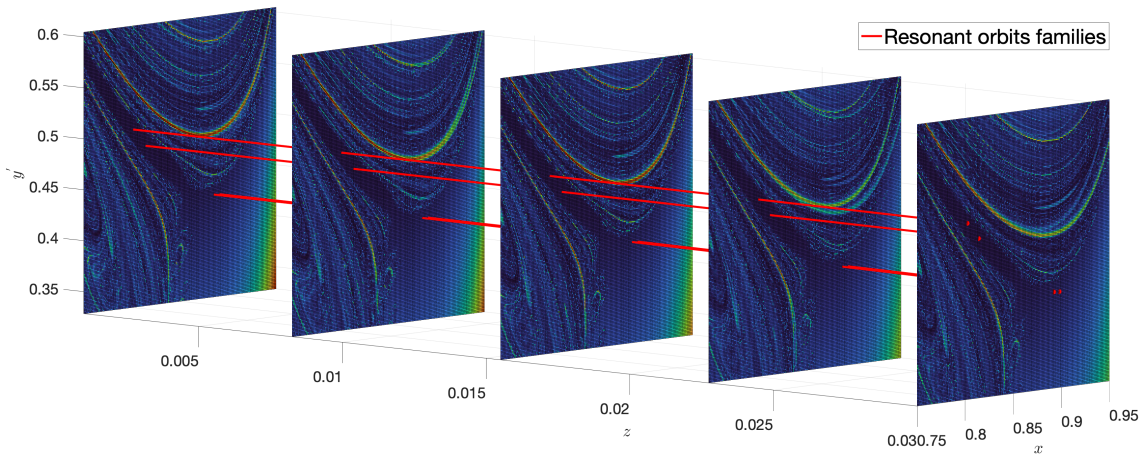

Figure 5.10: LD M_1 in the ER3BP at different z slices.

Another batch of samples points investigates the M_1 field in search of bounded orbits: three of them are picked in the central smooth channel and the other two at its sides.

Figure 5.11 shows that, in the $z = 0.03$ slice of the LD field, samples A, B, and E evolve in a similar fashion, while C and D diverge. Their ICs are listed in Table 5.4, and the trajectories are shown in the three different projections in Fig. 5.12.

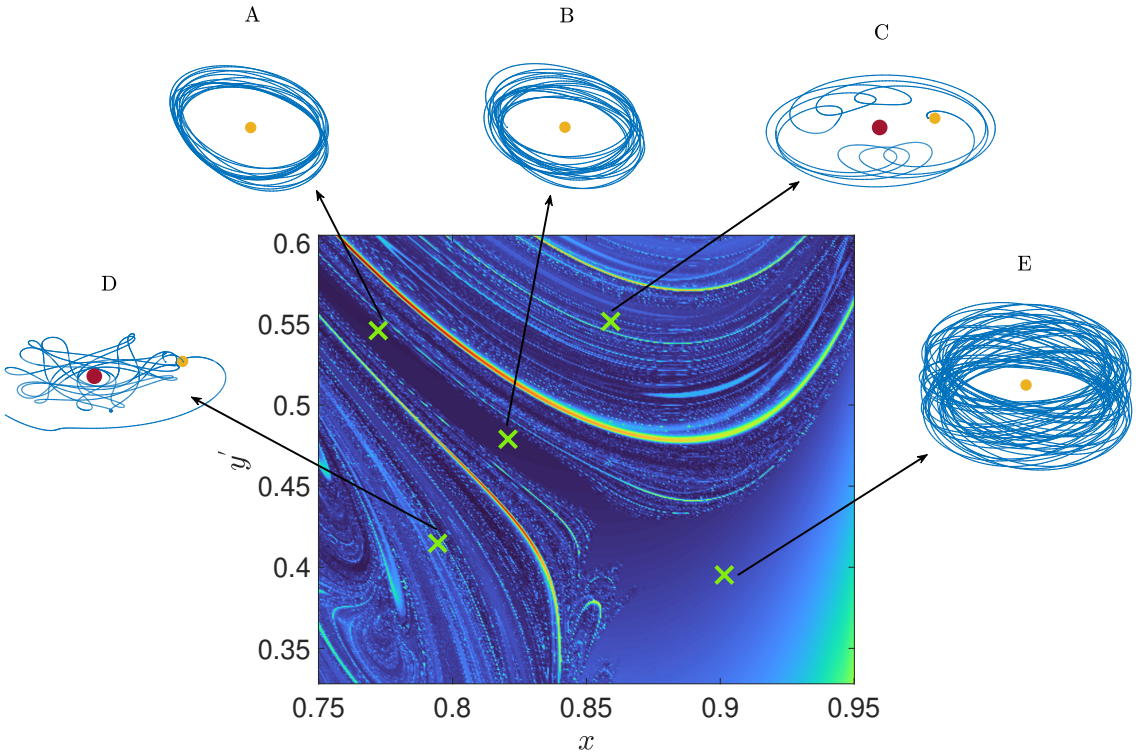

Figure 5.11: M_1 sampling in the ER3BP. The red and yellow dots are Didymos and Dimorphos not to scale, respectively.

Table 5.4: Orbits ICs in the ER3BP.

Orbit	Initial conditions, $f_0 = 0$						**Motion**
	x_0	y_0	z_0	$x_0^{'}$	$y_0^{'}$	$z_0^{'}$	
A	0.772222	0	0.03	0	0.545933	0	Bounded
B	0.820707	0	0.03	0	0.478967	0	Bounded
C	0.859090	0	0.03	0	0.551513	0	Escape
D	0.794444	0	0.03	0	0.414792	0	Escape
E	0.901515	0	0.03	0	0.395261	0	Bounded

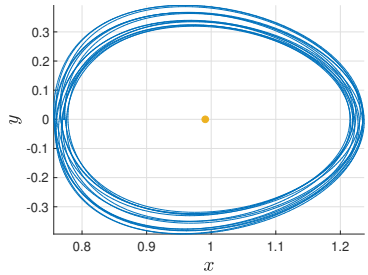

(a) A: xy-plane.

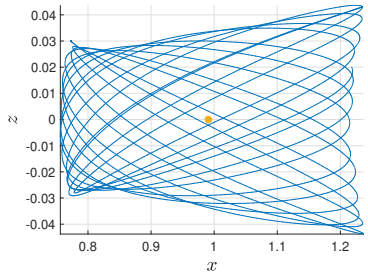

(b) A: xz-plane.

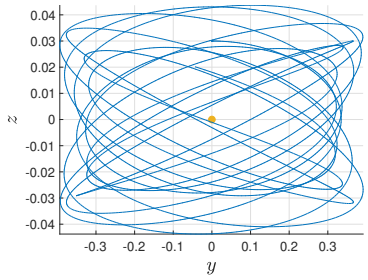

(c) A: yz-plane.

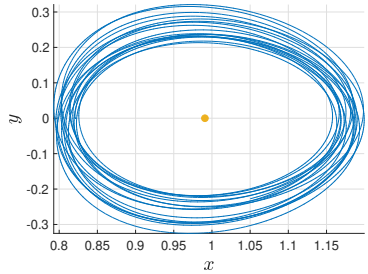

(d) B: xy-plane.

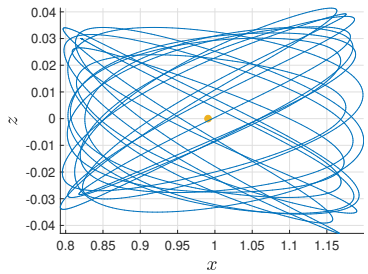

(e) B: xz-plane.

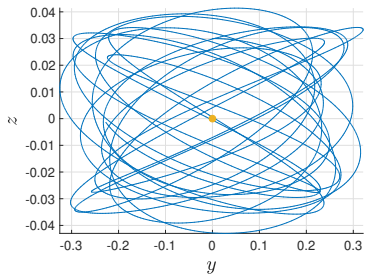

(f) B: yz-plane.

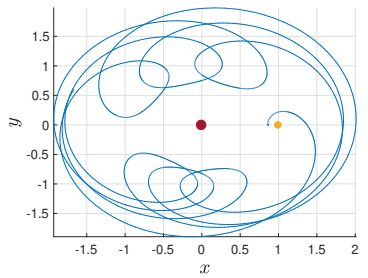

(g) C: xy-plane.

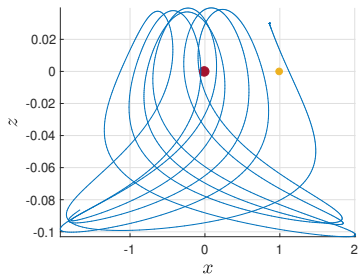

(h) C: xz-plane.

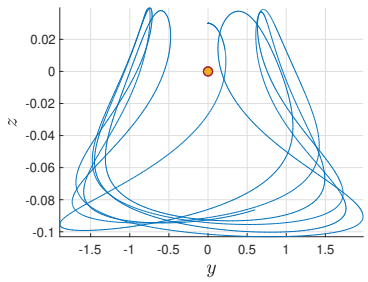

(i) C: yz-plane.

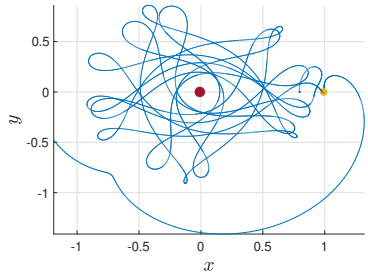

(j) D: xy-plane.

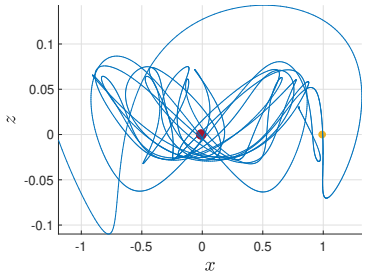

(k) D: xz-plane.

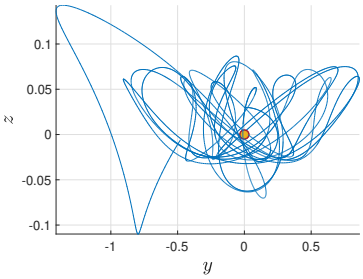

(l) D: yz-plane.

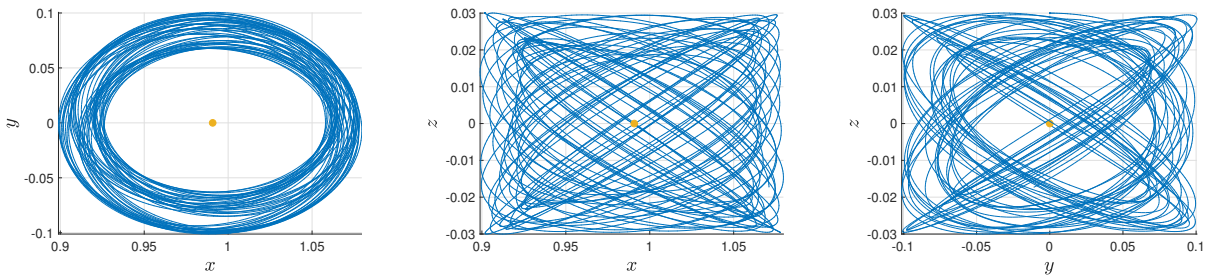

(m) E: xy-plane. (n) E: xz-plane. (o) E: yz-plane.

Figure 5.12: Samples evolution in the ER3BP. The red and yellow dots are Didymos and Dimorphos not to scale, respectively. For a better orbits representation, data units are not the same along each axis.

5.2.3. Sampling in the bi-elliptic restricted four-body problem

The presence of the Sun is examined in the bi-elliptic restricted four-body problem ($\beta = 0$ in Eq. (3.1)): the goal is to qualitatively study how its presence alters the structures already found. The Didymos–Dimorphos double asteroids system is assumed to be at the pericenter ($\theta_0 = 0$) of its heliocentric orbit: this is the worst-case scenario, where the gravitational pull of the Sun reaches its maximum. Therefore, in this region of space, the previously discovered structures would undergo the largest modifications.
The evolution along the z-direction is shown in Fig. 5.13.

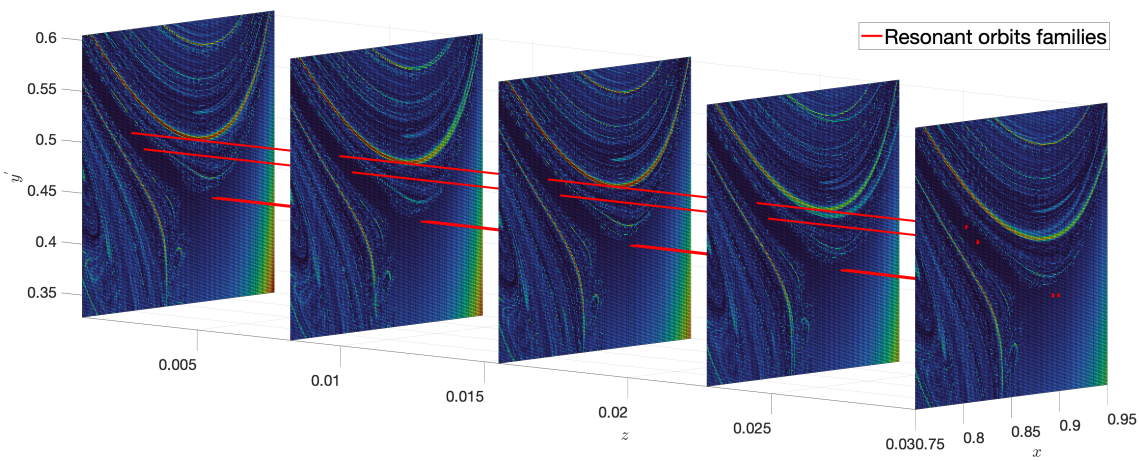

Figure 5.13: LD M_1 in the BER4BP, for $\theta_0 = 0$, at different z slices.

The outlines of the structures appear to be weakly affected by the gravitational influence of the Sun. Indeed, only faint alterations can be pointed out: the broad smooth region remains, and the borders with the chaotic areas come closer to each other, narrowing the channel dimension and, therefore, reducing the selection of orbits with bounded motion. As in the previous case, there are no significant changes in the evolution along the z-axis. The sampling typology retraces the previous case, with three points in the stable region (A, B, and E) and two points in the unstable ones (C and D), as shown in Fig. 5.14.

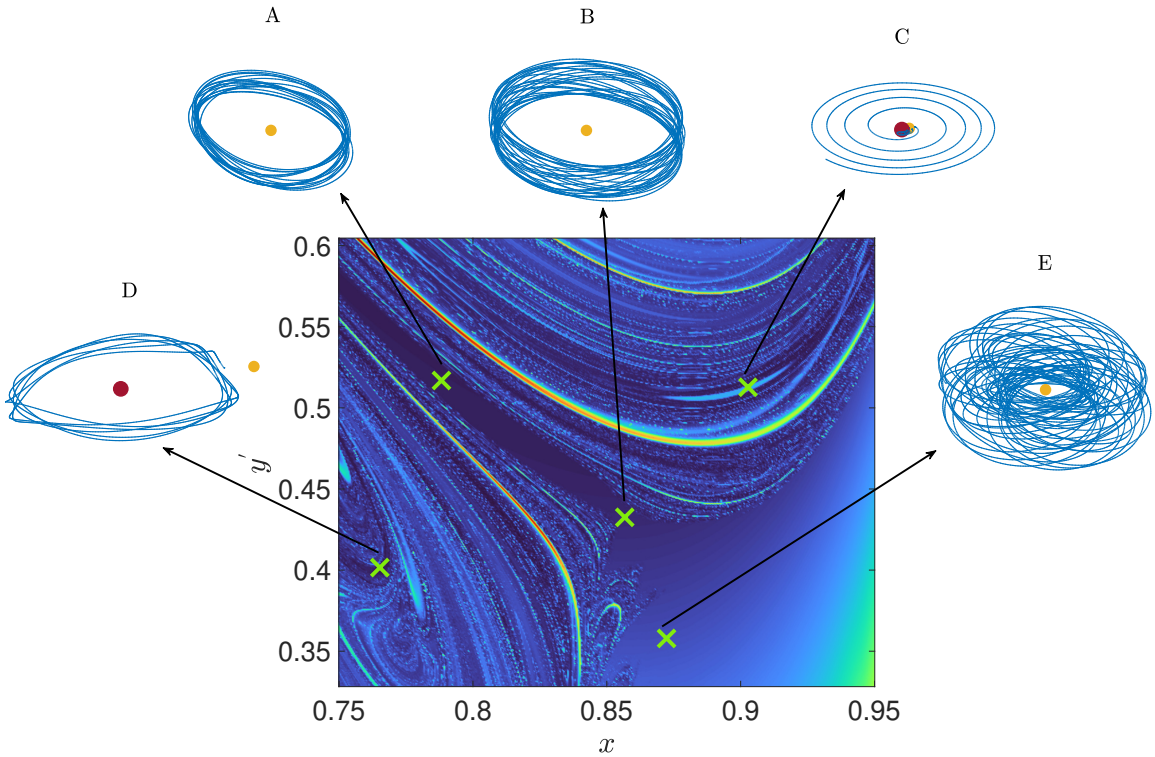

Figure 5.14: M_1 sampling in the BER4BP, with $\theta_0 = 0$. The red and yellow dots are Didymos and Dimorphos not to scale, respectively.

Orbit A, B, and E remains confined in the vicinity of Dimorphos, a sign that confirms the weak impact of the Sun over the LD structure. As they belong to the chaotic regions, trajectories C and D escape. Their ICs are listed in Table 5.5, and the trajectories are shown in the three different projections in Fig. 5.15.

Table 5.5: Orbits ICs in the BER4BP, $\theta_0 = 0$.

Orbit	Initial conditions, $f_0 = 0$						**Motion**
	x_0	y_0	z_0	$x_0^{'}$	$y_0^{'}$	$z_0^{'}$	
A	0.788238	0	0.03	0	0.516875	0	Bounded
B	0.856707	0	0.03	0	0.432539	0	Bounded
C	0.902753	0	0.03	0	0.512727	0	Escape
D	0.765215	0	0.03	0	0.401570	0	Escape
E	0.872322	0	0.03	0	0.357882	0	Bounded

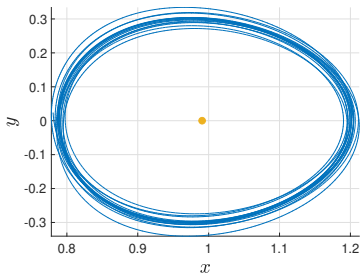

(a) A: xy-plane.

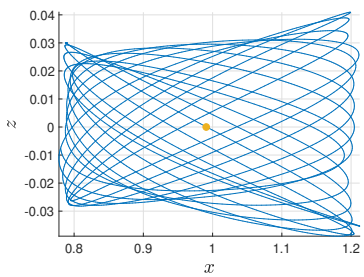

(b) A: xz-plane.

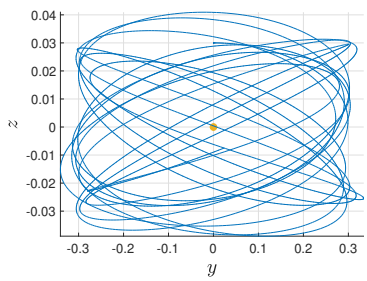

(c) A: yz-plane.

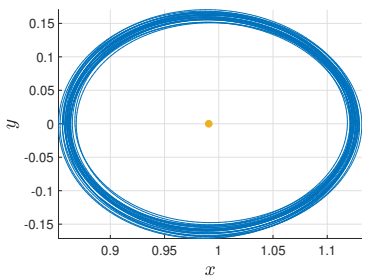

(d) B: xy-plane.

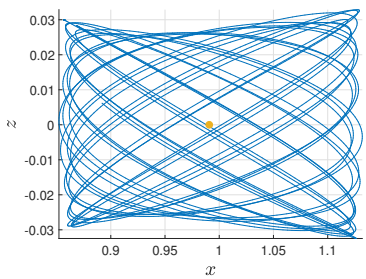

(e) B: xz-plane.

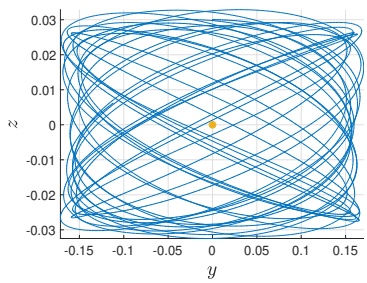

(f) B: yz-plane.

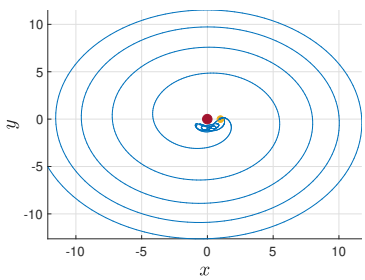

(g) C: xy-plane.

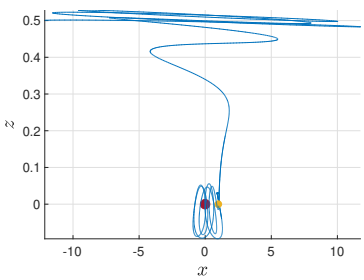

(h) C: xz-plane.

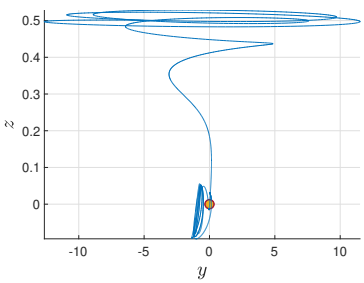

(i) C: yz-plane.

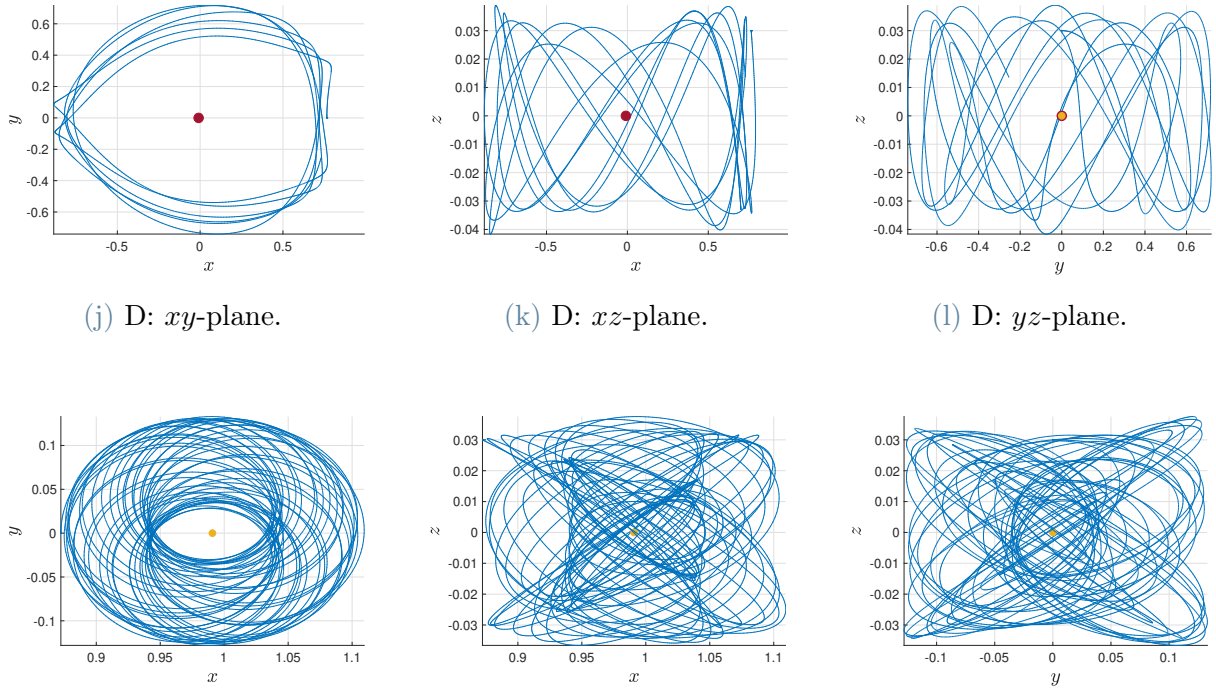

(j) D: xy-plane. (k) D: xz-plane. (l) D: yz-plane.

(m) E: xy-plane. (n) E: xz-plane. (o) E: yz-plane.

Figure 5.15: Samples evolution in the BER4BP. The red and yellow dots are Didymos and Dimorphos not to scale, respectively. For a better orbits representation, data units are not the same along each axis.

5.2.4. Sampling in the perturbed bi-elliptic restricted four-body problem

Finally, the effect of the SRP is addressed in a more realistic model: the SRP perturbed bi-elliptic restricted four-body problem. Previous research on the magnitude of such an acceleration concluded that it contributes significantly to the active maneuvering costs required to control the attitude of a Cubesat [11].

Two cases are investigated, depending on the angular position θ_0 on the heliocentric orbit:

- Didymos–Dimorphos at the **pericenter** of the heliocentric orbit $\theta_0 = 0$, at 1.013 AU: this is the closest point to the Sun, where its perturbations are the greatest. The smooth region collecting ICs of bounded orbits is expected to be severely affected: the access to the vast selection of bounded orbits is likely to be no longer permitted.

- Didymos–Dimorphos at the **apocenter** of the heliocentric orbit $\theta_0 = \pi$, at 2.27 AU: at the farthest point from the Sun, it represents the best-case scenario as the magnitude of the perturbations is the lowest.

Figure 5.16 shows what the regions look like when the system is at the pericenter of the heliocentric orbit. The resulting LD field is heavily altered: it lacks a clear distinction among the different regions as the separatrices are no longer pronounced; the two chaotic zones merge as they expand, taking up the entire phase space and incorporating the central channel that collected bounded orbits. In addition, as there is no longer the smooth area, the four red lines representing ICs of spatial resonant orbits now intersect chaotic regions.

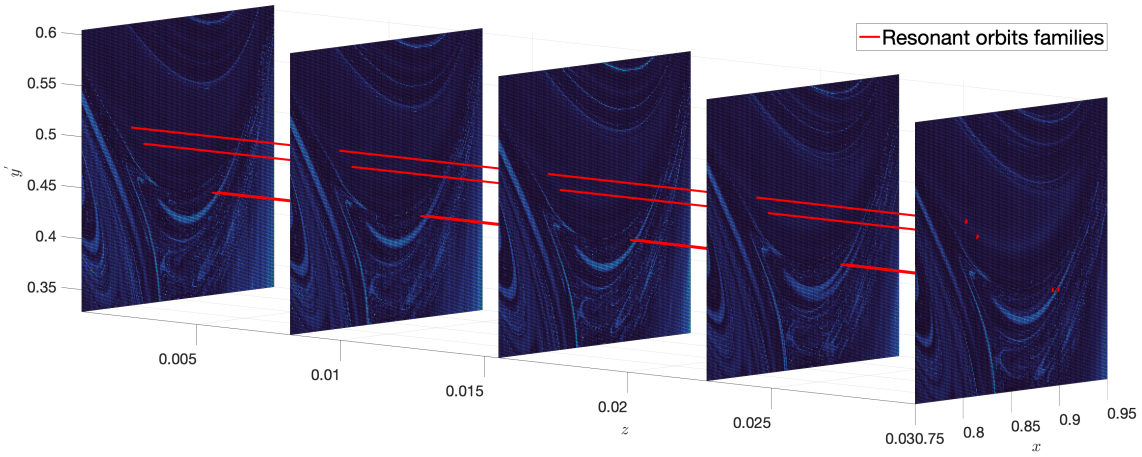

Figure 5.16: LD M_1 in the SRP perturbed BER4BP at different z slices, for $\theta_0 = 0$.

Searching for bounded orbits through sampling becomes more challenging. The first points (A, B) are sampled near the central channel's previous location to verify if a fraction of the smooth region is still accessible. Points C and D sample the two extended chaotic areas, and the final point E is chosen to be pretty close to the secondary Dimorphos to exploit its gravitational attraction as much as possible. The resulting orbits behavior is shown in Fig. 5.17. Almost all of the samples diverge: the effect of the SRP at the closest point to the Sun is so strong to sweep away any possible bounded motion, at least for the selected grid width. Sample E being so close to Dimorphos still revolves around it, but as already stated, physical impacts with the surface are not checked.

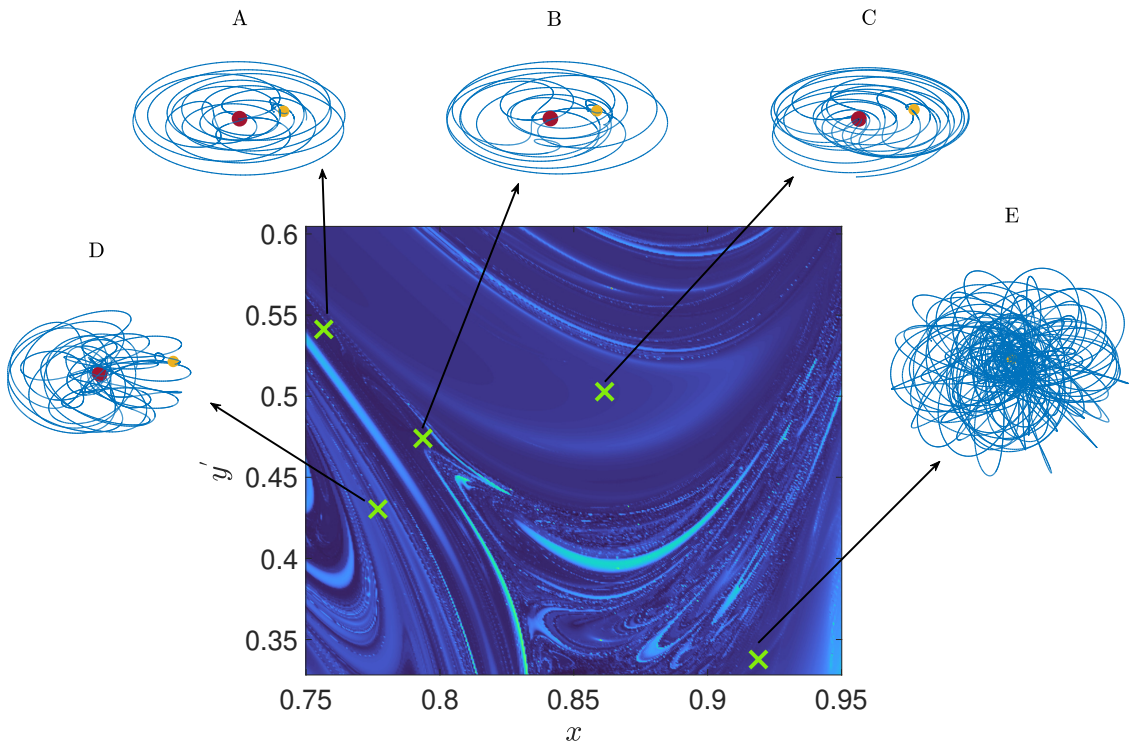

Figure 5.17: M_1 sampling in the SRP perturbed BER4BP, for $\theta_0 = 0$. The red and yellow dots are Didymos and Dimorphos not to scale, respectively.

ICs are listed in Table 5.6, and the trajectories are shown in the three different projections in Fig. 5.18.

Table 5.6: Orbits ICs in the SRP perturbed BER4BP, for $\theta_0 = 0$.

Orbit	Initial conditions, $f_0 = 0$						**Motion**
	x_0	y_0	z_0	x_0'	y_0'	z_0'	
A	0.756607	0	0.03	0	0.541208	0	Escape
B	0.793644	0	0.03	0	0.474016	0	Escape
C	0.861512	0	0.03	0	0.502773	0	Escape
D	0.776827	0	0.03	0	0.430419	0	Escape
E	0.918969	0	0.03	0	0.337697	0	Bounded

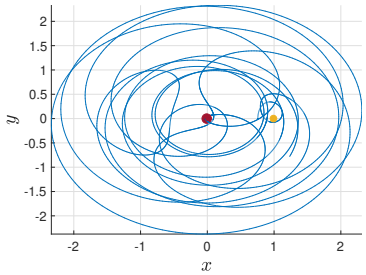

(a) A: xy-plane.

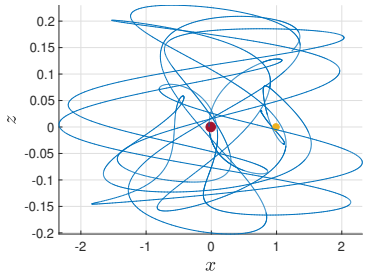

(b) A: xz-plane.

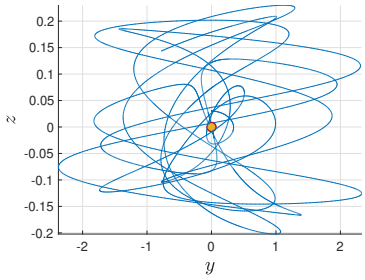

(c) A: yz-plane.

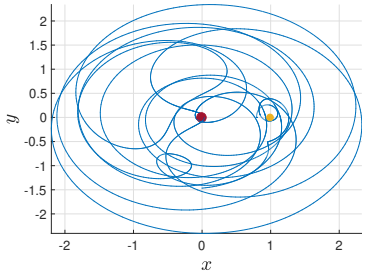

(d) B: xy-plane.

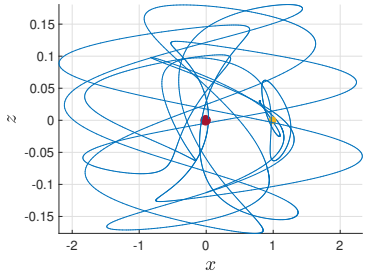

(e) B: xz-plane.

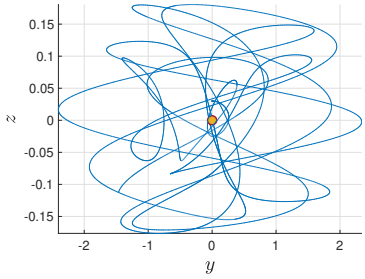

(f) B: yz-plane.

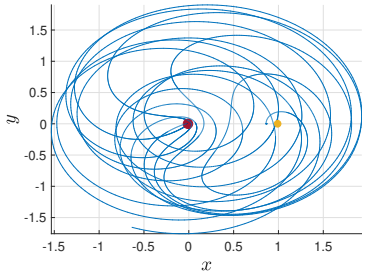

(g) C: xy-plane.

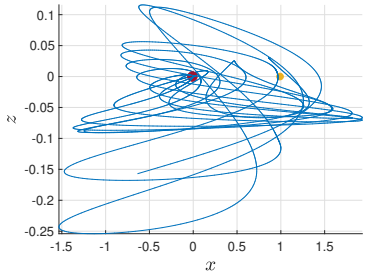

(h) C: xz-plane.

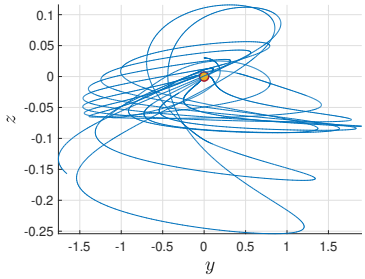

(i) C: yz-plane.

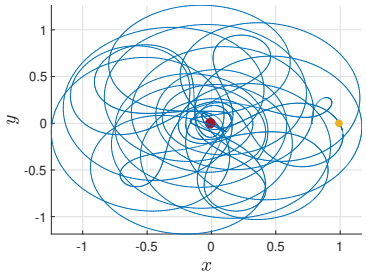

(j) D: xy-plane.

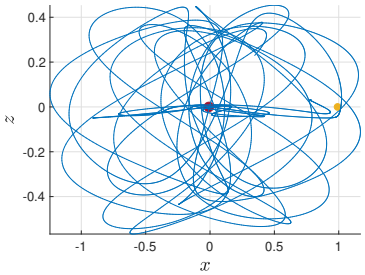

(k) D: xz-plane.

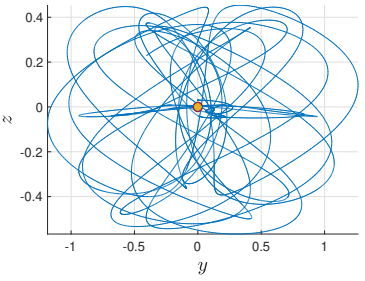

(l) D: yz-plane.

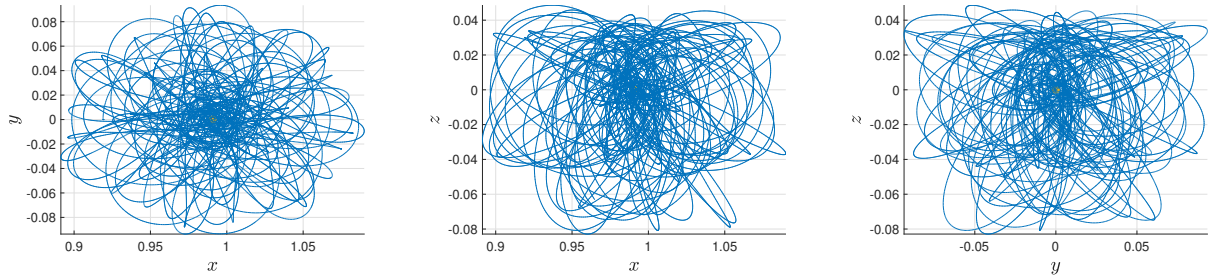

(m) E: xy-plane. (n) E: xz-plane. (o) E: yz-plane.

Figure 5.18: Samples evolution in the SRP perturbed BER4BP, for $\theta_0 = 0$. The red and yellow dots are Didymos and Dimorphos not to scale, respectively. For a better orbits representation, data units are not the same along each axis.

The best-case scenario, when the system is at the apocenter of its heliocentric orbit, is reported in Fig. 5.19. The area closer to Dimorphos in the bottom-right of the graph is the most affected by the evolution along z: stronger gradients emerge for lower values of z, and they disappear as z increases.

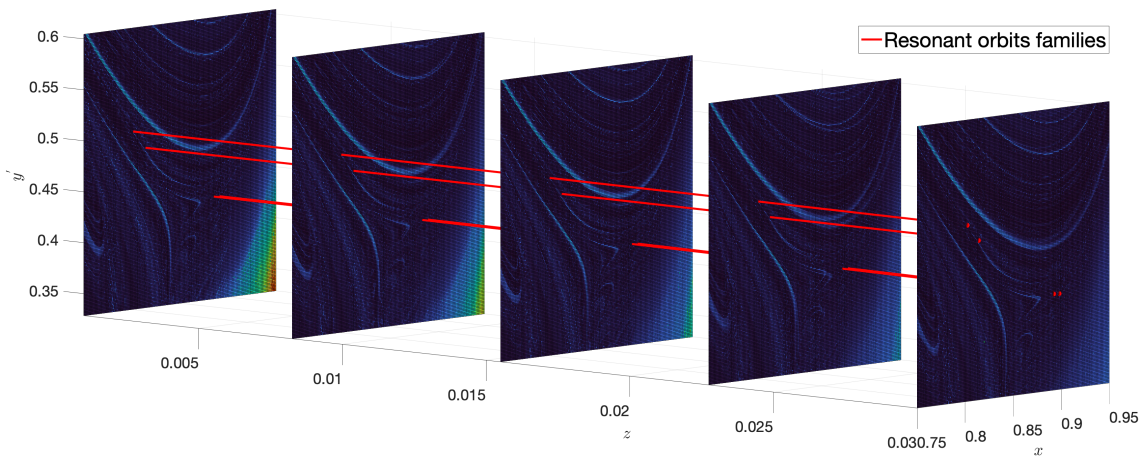

Figure 5.19: LD M_1 in the SRP perturbed BER4BP at different z slices, for $\theta_0 = \pi$.

The structure of the LD resembles, yet differently scaled, the case where the SRP is absent, with some differences to be noted. The entire smooth zone is broken down into two smaller regions, with chaotic behavior separating them. The first is a small portion of the channel that collects ICs of bounded orbits, in the top-left corner of the field: points A, B in Fig. 5.20 confirm the presence of stable orbits in this region once more, regardless

of the perturbations.

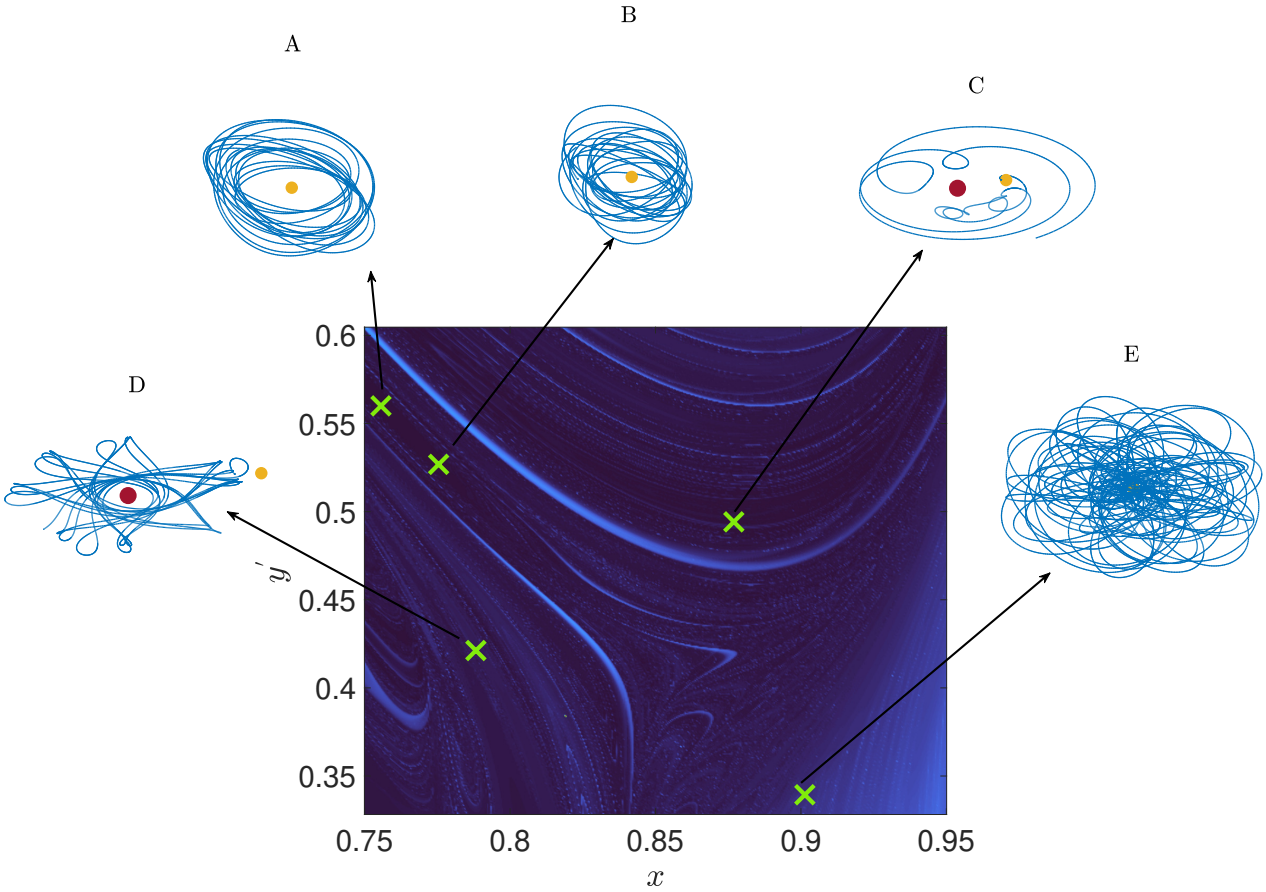

Figure 5.20: M_1 sampling in the SRP perturbed BER4BP, for $\theta_0 = \pi$. The red and yellow dots are Didymos and Dimorphos not to scale, respectively.

The second is the wide smooth area located on the bottom-right in which trajectory E, which flies very close to Dimorphos, is likely to impact the surface multiple times. Samples C and D, belonging to the unstable areas, immediately escape the system.
Surprisingly, when the system is at the pericenter of the heliocentric orbit, the stable regions vanish, only to reappear when the system travels away from the sun.
The collection of ICs is reported in Table 5.7 and the corresponding orbits are shown in the three different projections in Fig. 5.21.

Table 5.7: Orbits ICs in the SRP perturbed BER4BP, for $\theta_0 = \pi$.

Orbit	Initial conditions, $f_0 = 0$						**Motion**
	x_0	y_0	z_0	$x_0^{'}$	$y_0^{'}$	$z_0^{'}$	
A	0.755606	0	0.03	0	0.560010	0	Bounded
B	0.775425	0	0.03	0	0.526829	0	Bounded
C	0.876927	0	0.03	0	0.494201	0	Escape
D	0.788238	0	0.03	0	0.421203	0	Escape
E	0.901351	0	0.03	0	0.339356	0	Bounded

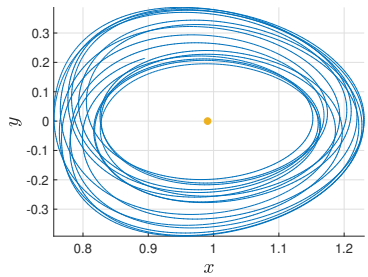

(a) A: xy-plane.

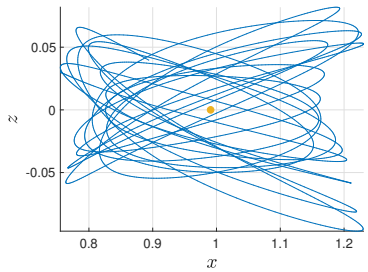

(b) A: xz-plane.

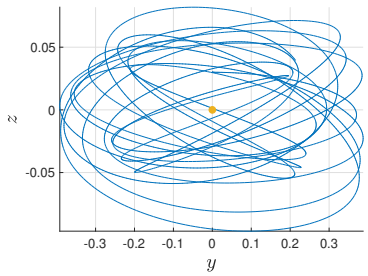

(c) A: yz-plane.

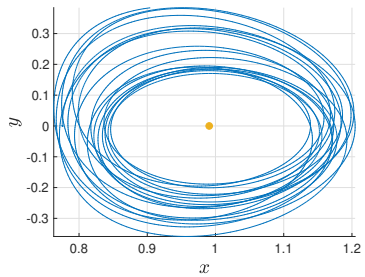

(d) B: xy-plane.

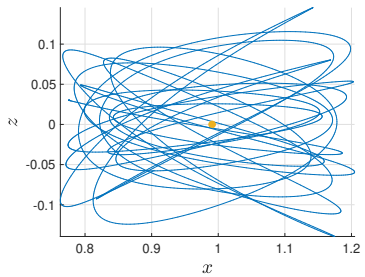

(e) B: xz-plane.

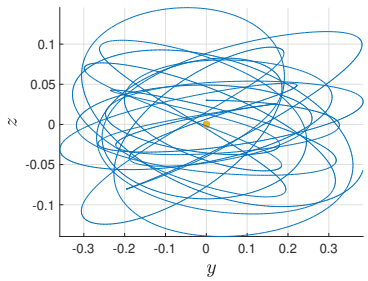

(f) B: yz-plane.

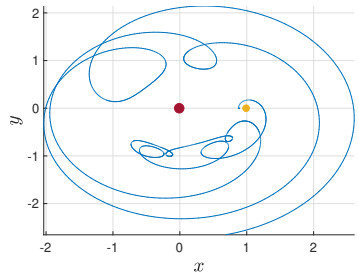

(g) C: xy-plane.

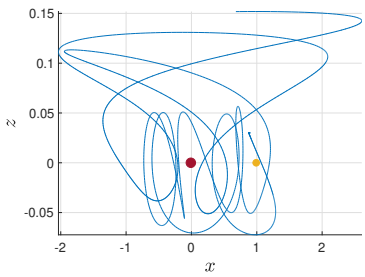

(h) C: xz-plane.

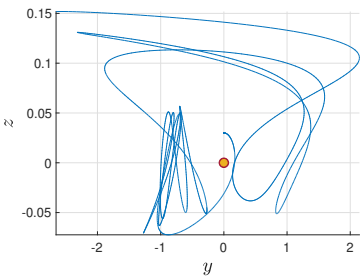

(i) C: yz-plane.

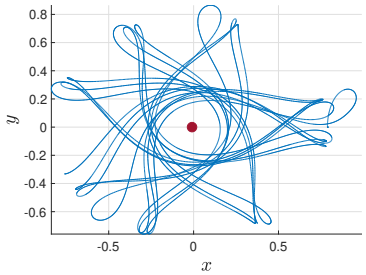

(j) D: xy-plane.

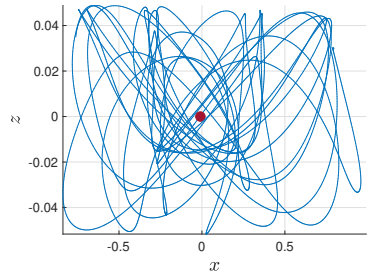

(k) D: xz-plane.

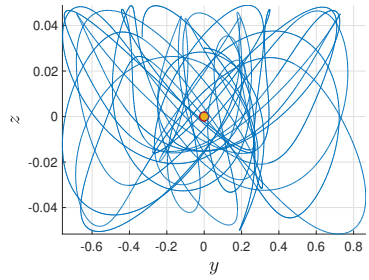

(l) D: yz-plane.

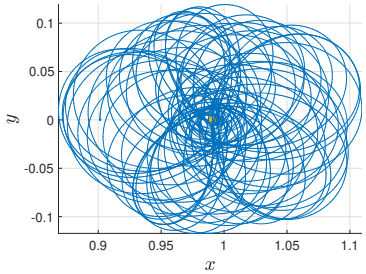

(m) E: xy-plane.

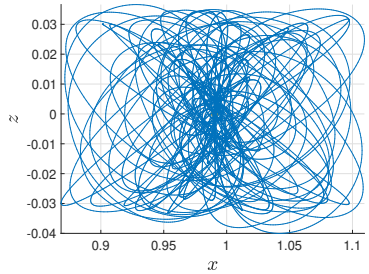

(n) E: xz-plane.

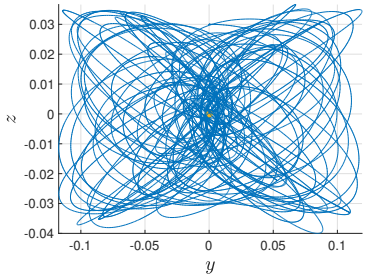

(o) E: yz-plane.

Figure 5.21: Samples evolution in the BER4BP, for $\theta_0 = \pi$. The red and yellow dots are Didymos and Dimorphos not to scale, respectively. For a better orbits representation, data units are not the same along each axis.

According to [22], LDs can effectively separate regions of different qualitative motions. This is confirmed through the numerous samples performed on the LD field.
When compared to other chaos indicators in literature, LDs stand out for their ease of use and computational efficiency. In fact, they can be calculated without propagation of the state transition matrix, unlike other methods like the FTLE field or the variational theory. This results in a faster computation because integrating thirty-six differential equations is no longer required. Instead, the number of equations to be integrated is determined by the number of LDs used.

6 | Final remarks

This main question was presented at the beginning of this work:

- *To what extent do Lagrangian descriptors provide insight into the highly chaotic environment by revealing the structures that organize the phase space into regions of different behavior?*

Research Objective. The final objectives of this dissertation are:

- *Find regions of bounded motion around the Didymos-Dimorphos binary system for a certain amount of time.*
- *Investigate the capability of the different Lagrangian descriptors to reveal organizing structures in astrodynamics systems.*
- *Classify the identified regions according to their qualitative behavior.*

LDs proved successful in identifying phase space organizing structures in binary asteroid environments. Yet, not all Lagrangian descriptors revealed capable of capturing dynamical information in the same way, at least for the problem at hand: the LD M_a was indeed unable to show any features associated with the different regions of motion. A follow-up study should look into whether this difference holds true when LDs are applied to other astrodynamics problems.

The features associated with the scalar field were inspected through DROs and resonant orbits, respectively for the planar and spatial case. Regions of bounded motion were found, for the selected grid width, almost in all of the implemented models. The smooth region containing ICs of bounded orbits, while easily recognizable in lower-fidelity models, shrinks and becomes less evident when the contribution of the SRP is accounted for. Indeed, as demonstrated, it totally vanishes when the system is at the pericenter of the heliocentric orbit, to re-appear only when further away from it.

The use of DROs and resonant orbits as identifiers actually proves redundant in models with no SRP, as simple sampling would have been sufficient to highlight the behavior of the different regions. However, when SRP comes into play, in particular when $\theta_0 = \pi$,

their role is crucial: identifying the two stable orbits merely through visual sampling would have been complicated without prior knowledge about the position of the stable regions. This justifies the use of periodic orbits as identifiers for the scalar field, which is then highly recommended.

When the search grid is enlarged, other regions containing initial conditions of bounded orbits may appear, at the cost of increased computational time, while maintaining the same resolution. A greater number of stable structures may emerge for shorter integration times, depending on the mission requirements, as this means less time for scientific operations.

An investigation of the robustness to the initial epoch f_0 and operational errors should be used to support the stability of the discovered orbits. This can be accomplished through Monte Carlo simulations that take into account the presence of errors caused by uncertainties. However, a small uncertainty about initial conditions should not be an issue for extensive bounded motion regions, as the solution would be qualitatively similar.

Overall, the results obtained from the application of Lagrangian descriptors to astrodynamic problems, and in particular in the search for quasi-periodic orbits, are promising. Moreover, they proved computationally faster and more efficient than other chaos indicators (the finite-time Lyapunov exponents and the variational theory of Lagrangian coherent structure, for instance) in exploring the rich dynamics of non-autonomous systems, as no propagation of the state transition matrix is required.
For these reasons, they can be considered a convenient and powerful tool in the preliminary stages of space missions design.

Bibliography

[1] N. Baresi, Z. Olikara, and D. Scheeres. Fully numerical methods for continuing families of quasi-periodic invariant tori in astrodynamics. *Journal of the Astronautical Sciences*, 65, 01 2018. doi:10.1007/s40295-017-0124-6.

[2] Battin and H. Richard. *An introduction to the mathematics and methods of astrodynamics*. American Institute of Aeronautics and Astronautics, 1999. doi:10.2514/4.861543.

[3] R. A. Broucke. Periodic orbits in the restricted three-body problem with Earth–Moon masses. Technical Report 32-1168, NASA, Jet Propulsion Laboratory, California Institute of Technology, Pasadena, California, 1968.

[4] R. A. Broucke. Stability of periodic orbits in the elliptic, restricted three-body problem. *AIAA*, 1969. doi:10.2514/3.5267.

[5] H. Chen, E. Canalias, D. Hestroffer, and X. Hou. Effective stability of quasi-satellite orbits in the spatial problem for Phobos exploration. *Journal of Guidance, Control, and Dynamics*, 43:2309–2320, 08 2020. doi:10.2514/1.G004911.

[6] G. T. Craven, A. Junginger, and R. Hernandez. Lagrangian descriptors of driven chemical reaction manifolds. *Physical Review E*, 2017. doi:10.1103/PhysRevE.96.022222.

[7] H. Curtis. *Orbital Mechanics for Engineering Students: Revised Reprint*. Butterworth-Heinemann, 2020. doi:10.1016/C2020-0-01873-6.

[8] A. S. Demian and S. Wiggins. Detection of periodic orbits in Hamiltonian systems using Lagrangian descriptors. *International Journal of Bifurcation and Chaos*, 2017. doi:10.1142/S021812741750225X.

[9] E. J. Doedel, R. C. Paffenroth, H. B. Keller, D. Dichmann, J. Galan-vioque, and A. Vanderbauwhede. Computation of periodic solutions of conservative systems with application to the 3-body problem. *International Journal of Bifurcation and Chaos*, 2003. doi:10.1142/S0218127403007291.

[10] F. Ferrari and M. Lavagna. Periodic motion around libration points in the Elliptic Restricted Three-Body Problem. *Nonlinear Dynamics*, 7 2018. doi:10.1007/s11071-018-4203-4.

[11] F. Ferrari, V. Franzese, M. Pugliatti, C. Giordano, and F. Topputo. Preliminary mission profile of Hera's Milani CubeSat. *Advances in Space Research*, 67(6):2010–2029, 2021. doi:10.1016/j.asr.2020.12.034.

[12] F. Ferrari, V. Franzese, M. Pugliatti, C. Giordano, and F. Topputo. Trajectory Options for Hera's Milani CubeSat Around (65803) Didymos. *Journal of the Astronautical Sciences*, 68(4):973–994, Dec. 2021. doi:10.1007/s40295-021-00282-z.

[13] G. Haller. A variational theory of hyperbolic Lagrangian coherent structures. *Physica D*, 2010. doi:10.1016/j.physd.2010.11.010.

[14] M. Henon. Numerical exploration of the restricted problem, V. *Astronomy and Astrophysics*, 1:223–238, Feb. 1969.

[15] X. Y. Hou and L. Liu. On motions around the collinear libration points in the elliptic restricted three-body problem. *Monthly Notices of the Royal Astronomical Society*, 2011. doi:10.1111/j.1365-2966.2011.18970.x.

[16] K. Howell and E. Campbell. Three-dimensional periodic solutions that bifurcate from halo families in the circular restricted three-body problem. *Advances in the Astronautical Sciences*, 102:891–910, 01 1999.

[17] K. C. Howell. Three-Dimensional Periodic Halo Orbits. *Celestial Mechanics*, 32(1): 53, Jan. 1984. doi:10.1007/BF01358403.

[18] N. Hyeraci and F. Topputo. Method to design ballistic capture in the elliptic restricted three-body problem. *Journal of Guidance, Control, and Dynamics*, 33:1814–1823, 11 2010. doi:10.2514/1.49263.

[19] S. H. Kellert and L. Sklar. In the wake of chaos: Unpredictable order in dynamical systems. *Philosophy of Science*, 64(1):181, 1997.

[20] W. S. Koon, M. W. Lo, J. E. Marsden, and S. D. Ross. *Dynamical Systems, the Three-Body Problem and Space Mission Design.* 1 edition, 2006. doi:10.1142/9789812792617_0222.

[21] N. Kwok, J.H. Periodic orbits of the elliptic restricted problem for the Sun–Jupiter–Saturn system. *Celestial mechanics*, 1982. doi:10.1007/BF01228948.

[22] A. M. Mancho, S. Wiggins, J. Curbelo, and C. Mendoza. Lagrangian de-

scriptors: A method for revealing phase space structures of general time dependent dynamical systems. *Commun. Nonlinear. Sci. Numer. Simulat.*, 2013. doi:10.1016/j.cnsns.2013.05.002.

[23] V. V. Markellos. Bifurcations of Planar to Three-Dimensional Periodic Orbits in the General Three-Body Problem. *Celestial Mechanics*, 25(1):3–31, Sept. 1981.

[24] B. McCarthy and K. Howell. Leveraging quasi-periodic orbits for trajectory design in cislunar space. *Astrodynamics*, 5, 01 2021. doi:10.1007/s42064-020-0094-5.

[25] C. Mendoza and A. M. Mancho. Hidden geometry of ocean flows. *Physical Review Letters*, 2010. doi:10.1103/PHYSREVLETT.105.038501.

[26] G. H. Mohammad Farazmand. Erratum and addendum to "a variational theory of hyperbolic Lagrangian coherent structures". *Physica D*, 2011. doi:10.1016/j.physd.2011.09.013.

[27] S. Naik, V. J.García-Garrido, and S. Wiggins. Finding NHIM: Identifying high dimensional phase space structures in reaction dynamics using Lagrangian descriptors. *Commun. Nonlinear. Sci. Numer. Simulat.*, 2019. doi:10.1016/j.cnsns.2019.104907.

[28] Z. Olikara and D. Scheeres. Numerical method for computing quasi-periodic orbits and their stability in the restricted three-body problem. *Advances in the Astronautical Sciences*, 145:911–930, 01 2012.

[29] J. Parker, K. Davis, and G. Born. Chaining periodic three-body orbits in the Earth–Moon system. *Acta Astronautica - Acta Astronaut*, 67:623–638, 09 2010. doi:10.1016/j.actaastro.2010.04.003.

[30] F. Revuelta, M. Benito, and F. Borondo. Unveiling the chaotic structure in phase space of molecular systems using Lagrangian descriptors. *Physical Review E*, 2019. doi:10.1103/PhysRevE.99.032221.

[31] I. A. Robin. Bifurcations of plane with three-dimensional periodic orbits in the elliptic restricted problem. *Celestial Mechanics and Dynamical Astronomy*, 1981. doi:10.1007/BF01228548.

[32] I. A. Robin and V. Markellos. Numerical determination of three-dimensional periodic orbits generated from vertical self-resonant satellite orbits. *Celestial Mechanics and Dynamical Astronomy*, 1980. doi:10.1007/BF01231276.

[33] A. E. Roy and M. W. Ovenden. On the occurrence of commensurable mean motions

in the solar system. The mirror theorem. *Monthly Notices of the Royal Astronomical Society*, 1955. doi:10.1093/mnras/115.3.296.

[34] A. Ruiz-Herrera. Some examples related to the method of Lagrangian descriptors. *Chaos 25*, 2015. doi:10.1063/1.4922182.

[35] C. J. Scott and D. B. Spencer. Calculating transfer families to periodic distant retrograde orbits using differential correction. *Journal of Guidance, Control, and Dynamics*, 33(5):1592–1605, 2010. doi:10.2514/1.47791.

[36] J. E. M. Shawn C. Shadden, Francois Lekienb. Definition and properties of Lagrangian coherent structures from finite-time Lyapunov exponents in two-dimensional aperiodic flows. *Physica D*, 2005. doi:10.1016/j.physd.2005.10.007.

[37] S. Soldini. *Design and Control of Solar Radiation Pressure Assisted Missions in the Sun-Earth Restricted Three-Body Problem*. PhD thesis, 06 2016.

[38] V. Szebehely and G. E. O. Giacaglia. On the elliptic restricted problem of three bodies. *Astronomical Journal*, 69:230, Apr. 1964. doi:10.1086/109261.

[39] F. Topputo. Fast numerical approximation of invariant manifolds in the circular restricted three-body problem. *Communications in Nonlinear Science and Numerical Simulation*, 2015. doi:10.1016/j.cnsns.2015.08.004.

[40] P. Verrier, T. Waters, and J. Sieber. Evolution of the L1 halo family in the radial solar sail CRTBP. *Celestial Mechanics and Dynamical Astronomy*, 120, 08 2013. doi:10.1007/s10569-014-9575-2.

[41] Y. Yu, P. Michel, S. R. Schwartz, S. P. Naidu, and L. A. Benner. Ejecta cloud from the AIDA space project kinetic impact on the secondary of a binary asteroid: I. mechanical environment and dynamical model. *Icarus*, 282:313–325, 2017. ISSN 0019-1035. doi:10.1016/j.icarus.2016.09.008.